Crustal structure of the Northeast South China Sea rifted margin

*Mateus Rodrigues de Vargas[1]
Julie Tugend[1,2]
Geoffroy Mohn[1]
Nick Kusznir[3]
Lin Liang-Fu [4]

corresponding author: mrvargas1989@gmail.com
[1] Géosciences et Environnement Cergy (GEC), CY Cergy Paris Université, Neuville-sur-Oise, France
[2] Commission for the Geological Map of the World, Paris, France
[3] Department of Earth, Ocean and Ecological Sciences, University of Liverpool, Liverpool, United Kingdom
[4] Ocean Center, National Taiwan University, Taipei, Taiwan

ABSTRACT

We investigate the crustal structure of the NE South China Sea (SCS) margin to constrain its crustal thickness and basement nature with implications for the Mesozoic and Cenozoic evolution of the SCS. First-order interfaces interpreted from seismic reflection data were integrated into a 3D gravity inversion scheme to determine Moho depth and crustal thickness variations. A joint inversion of seismic and gravity data allowed us to determine crustal density variations along 2D profiles. The distal margin is divided into two distinct crustal domains: the Southern Rift System (SRS), and Southern High (SH). The SRS shows an extremely thinned continental crust on top of which thick Cenozoic sequences are observed. It is separated from the oceanic crust (~ 6 to 8 km thick) by the SH, a comparatively thicker crust (~ 10 to 15 km thick) with numerous magmatic additions. The distal NE SCS margin formed during the Cenozoic rifting of the SCS. The crust of the SH likely corresponds to a polygenic crust, recording polyphase magmatic activity since the Mesozoic, with potentially significant activity during Cenozoic post-rift time. The NE SCS margin is conjugate to Palawan, whose basement is interpreted to be part of the exotic Luconia microcontinent that collided with Eurasia during the Late Cretaceous. Basement similarities between Palawan and the SH are highlighted, suggesting that the latter might also be part of Luconia. Our results suggest that the suture between Eurasia and Luconia might have acted as a preferred zone for the Cenozoic rift development.

KEY-POINTS

- The Northeastern South China Sea rifted margin shows a contrasted crustal structure constrained by seismic and gravity data.

- Part of the distal margin corresponds to a dense polygenic crust that underwent polyphase magmatic activity.

- The former Mesozoic suture zone between Eurasia and Luconia acted as a weakness zone for the Cenozoic rifting.

1. INTRODUCTION

The South China Sea (SCS) has experienced a series of geodynamic events both before and after its Cenozoic opening, which have played a major role in shaping its present-day structure (Sibuet et al., 2016; Taylor and Hayes, 1983; Wang et al., 2014). The SCS serves as a natural case study for investigating the rifting tectonics and the effects of pre- and post-rift events on the crustal structure of a continental rifted margin. In this study, we focus on the northeast segment of the SCS rifted margin (NE SCS) characterized by different structural domains, whose nature and pre-rift paleogeographic affinity are still poorly constrained (McIntosh et al., 2014; Pubellier et al., 2016; Sibuet et al., 2016; Taylor and Hayes, 1983).

The crustal structure of the NE SCS distal margin is particularly contrasted, being characterized by a hyper-thinned crust separated from the unambiguous oceanic crust by a domain of thicker crust (Eakin et al., 2014; Lester et al., 2014; S. Liu et al., 2018; Liu et al., 2021, 2023). The hyper-thinned crustal domain has been interpreted as continental crust possibly associated with or without local mantle serpentinization underneath (Eakin et al., 2014; Lester et al., 2014; S. Liu et al., 2018; Liu et al., 2021, 2023) or as Cenozoic oceanic crust (Hsu et al., 2004; Sibuet et al., 2004, 2002; Yeh et al., 2010). The thicker piece of crust located further south (i.e., Southern High) is interpreted either as having a mafic nature (Hsu et al., 2004; Reed, 1995; Sibuet et al., 2016; Xu et al., 2022; Yeh et al., 2012, 2010) or a continental nature interspersed with magmatic additions (Bautista et al., 2001; Fan et al., 2017; Lester et al., 2014; Liu et al., 2023, 2021; Sibuet et al., 2016).

This study aims to constrain the nature, age, and formation processes of the distal NE SCS margin. To achieve this goal, we compiled data from vintage and recent seismic reflection, refraction, dredges, and drilling results. We applied a gravity-inversion scheme to calculate 3-D Moho depth and crustal thickness variations and used a joint inversion of gravity and seismic data to determine crustal density variations along a set of 2-D profiles. The resulting geophysical properties are analyzed together with geological and petrological data to test different scenarios for the nature of the crust of the NE SCS margin and evaluate potential paleogeographic implications.

The continental crust of the proximal margin shows evidence of an Eurasian affinity (Chen et al., 1997; Lin et al., 2003). The distal NE SCS rifted margin has previously been interpreted as oceanic crust from the Proto-Pacific (e.g., the Mesozoic plateau of Xu et al., 2022), Proto-South China (e.g., Sibuet et al., 2016), Philippine Sea Plate (Hsu et al., 2004). Alternative interpretations suggest a continental nature of Eurasian affinity (e.g., Lin et al., 2003) or linked to the cryptic Luconia block (e.g., Holloway, 1981; Taylor and Hayes, 1983).

Our results suggest that the crust of the NE SCS distal margin likely corresponds to polygenic continental crust that recorded multi-episodic magmatic activity at least since the Mesozoic, with significant activity during Cenozoic post-rift time.

2. GEOLOGICAL BACKGROUND

The South China Sea (SCS) is a marginal sea located in the Western Pacific with a long-lasting history ranging from the accretion of Paleo-Mesozoic terranes, Paleogene to Neogene rift and oceanic propagation, and Neogene to Present subduction (Figure 1A) (Wang et al., 2014).

The SCS continental basement limiting the oceanic domain is currently divided into three main terranes: Indochina, South China, and Luconia (Pubellier and Sautter, 2022; Sautter and Pubellier, 2022). Indochina is located to the West of the SCS and is bounded to the South China terrane by the Red River Fault System (Figure 1A). These two terranes are part of Eurasia and include, among others, Mesozoic arc-related granitoids found throughout the Pearl River Mouth Basin, Macclesfield Bank, and Spratly Islands generated by processes analogous to the Andean and Western-Pacific settings (Chen et al., 2010; Fan et al., 2022; Shao et al., 2007; Webb et al., 2023; Ye et al., 2018; Zhou et al., 2008). To the South, several studies reported the occurrence of an “exotic” microcontinent referred to as Luconia (e.g., Holloway, 1981), which has been accreted to Eurasia during the Mesozoic although its exact provenance and evolution remain poorly constrained (Figure 1A) (Fan et al., 2022; Hall and Breitfeld, 2017; Knittel, 2011; Webb et al., 2023).

From the Late Cretaceous onwards, the SCS heterogeneous continental crust was subject to extension that caused a wide-rifting architecture with a general N-S to NE-SW trend. The timing of this rifting varies from the NE to the SW. In the NE SCS, the syn-rift stage spans from Paleocene to Eocene (e.g., Penghu, Pearl River Mouth, and Tainan basins), while in the SW SCS, this syn-rift stage mostly occurs from Eocene to early Miocene (e.g., Phu Khan Basin) (Figure 1B) (Fan et al., 2022; Hu et al., 2013; Morley, 2016; Rizzi et al., 2021; Sibuet et al., 2016; Wang et al., 2014, 2015; Weilin et al., 2019).

The onset of seafloor spreading started during the early Oligocene in the East Subbasin (ca. 33 to 32 Ma), propagated to the SW Subbasin in the early Miocene (ca. 26-23 Ma) (Briais et al., 1993; Li et al., 2014; Taylor and Hayes, 1983), and ceased in the late Miocene (ca. 15 Ma) (Figure 1A and B) (Briais et al., 1993; Li et al., 2014; Taylor and Hayes, 1983). From Paleogene to present, during the syn to post-rift stages, diffuse magmatic pulses occurred (Chen et al., 2010; Fan et al., 2017; Juang and Chen, 1992; Lei et al., 2018; Sun et al., 2010; Tian et al., 2019; Wang et al., 2012a; Zhang et al., 2016; Zhong et al.,

2018) (Figure 1B). This diffuse magmatism occurred both in the continental and oceanic domains and oftentimes is related to the evolution of various seamounts (Fan et al., 2017).

From the middle Miocene to the present, the oblique convergence between Eurasia (W) and the Philippines plates (E) (i.e., the South China Sea and the Luzon Arc, respectively) generated a subduction system that is delimited by the Manilla Trench (Figure 1A and B) (Taylor and Hayes, 1983). East of this trench, several compressive structures form an elongated N-S accretionary prism. In its northernmost part, this compression led to the uplift of Taiwan Island during the last ca. 6 Ma (Figure 1B) (Lin et al., 2003).

Northwest of the Manila trench, the Northeast South China Sea (NE SCS) rifted margin occurs (Figure 1C). This margin is herein defined as a geological entity that encompasses a **proximal margin** (Nanjihtao, Taihsi, and Penghu basins – i.e., Northern Rift System), the Tainan Basin sensu strictu (i.e., Northern Low and Central High; Lee et al., 1993) and **distal margin** (SW Taiwan Basin; Wu, 1985 - i.e., Southern Rift System and Southern High).

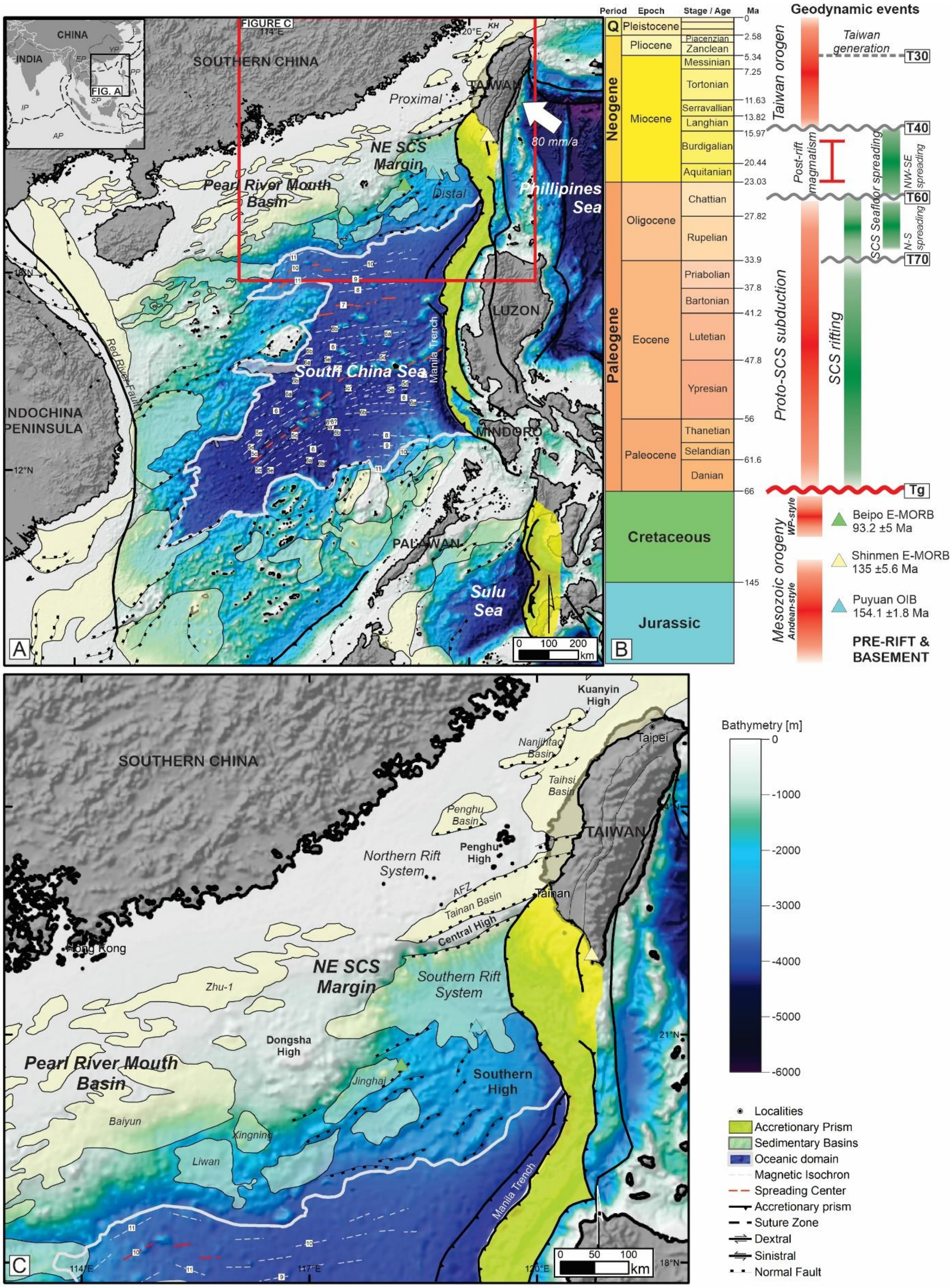

Figure 1. (A) Simplified geological map of the South China Sea, its main structures, and sedimentary basins. Plate boundaries (upper-left, black-dashed line) according to Bird (2003). IP – India Plate, EP – Eurasia Plate, SP – Sunda Plate, YP - Yangtze Plate, PP – Philippines Plate, AP – Australian Plate; AFZ – A fault zone. The big white arrow represents the present-day mean annual velocity vector of the Philippine Plate, according to Seno(1977) and Yu et al.(1997). The red rectangle is the area presented in 1C. (B) Simplified geodynamic chart with the main events in the NE SCS. Triangles represent the

location of Mesozoic-aged seamounts dated by Xu et al. (2022) and Tian et al.(2019). (C) The NE South China Sea Margin, adjacent units, and main structural highs. Structural units in A and C (i.e., structures, magnetic isochrons, accretionary prism, sedimentary basins, and oceanic domain) are according to Briais et al. (1993), Pubellier et al. (2016); Xie et al. (2019); Yan et al. (2020), and this work.

2.1 The structure of the NE SCS Margin

The NE SCS Margin is characterized by a system of Paleocene to early Oligocene NE-trending structures such as grabens, half-grabens, and structural highs with wedge-shaped architecture (Figure 1C) (Lester et al., 2014; Yeh et al., 2012). These wedge-shaped basins are associated with rifting that later on generated the South China Sea oceanic crust (Taylor and Hayes, 1983). This extensional system is widely overlaid by Oligocene to Miocene passive margin sedimentation interfingered with Paleocene-Eocene and Miocene post-rift volcanism events (Figure 1B) (Lin et al., 2003). Volcanism is geographically wide, occurring in clusters such as in the Penghu Islands (events of 65 to 58 Ma, 42 to 36 Ma, and 17 to 8 Ma) (Chung et al., 1994; Juang and Chen, 1992; Wang et al., 2012a), Taiwan Strait (56 to 48 Ma) (Wang et al., 2012a), NW and SW Taiwan (23 to 9 Ma and 15 Ma, respectively) (Chung et al., 1994; Smith and Lewis, 2007), and in Puyuan-Formosa Seamount (22 to 21 Ma) (Figure 1C) (Wang et al., 2012b). Younger basin-forming processes related to the Taiwan fold and thrust belt, as observed in the Nanjihtao Basin (Lin et al., 2003), are also considered part of the NE SCS Margin (Figure 1B).

The continental crust of the NE SCS Margin is characterized by contrasting crustal architectures. North of the A fault zone (AFZ) (Figure 1C), the crust is thick (> 25 km) (Gozzard et al., 2019; Lester et al., 2014; Lin et al., 2021) and likely composed of Paleo- to Mesozoic metamorphic and igneous rock assemblage overlaid by Mesozoic (meta)sediments (Chen et al., 2010; Lin et al., 2003; Lin and Chen, 2016; Taylor and Hayes, 1983). In this area, several isolated Paleocene to Eocene rift basins (i.e., Penghu, Taihsi, and Nanjihtao) (Lin et al., 2003) occur, characterizing the Northern Rift System (NRS) of the **Proximal Margin** (Figure 1C). Between AFZ and the Central High, occurs the Tainan Basin (Figure 1C) (Lin et al., 2003). South of this region, the crust progressively thins, reaching values that range from ca. 15 km to 6 km up to the oceanic crust (Lester et al., 2014), thereby characterizing the **Distal Margin**, where the Southern Rift System (SRS) and the Southern High (SH) occur (Figure 1C).

The SRS, which corresponds to the SW Taiwan Basin (Wu, 1985), is hypothesized to consist of either a hyper-thinned continental crust under which mantle serpentinization might occur (Liu et al., 2023, 2021), or an Eocene oceanic crust (Hsu et al., 2004) (Figure 1C). The onset of rifting for this region is unclear, but at least older than early Oligocene (Lester et al., 2014; McIntosh et al., 2014; Yeh et al., 2010, 2012), or late Eocene (Hsu et al., 2004).

Further to the south, the SRS is bounded by the SH (Figure 1C). This area is characterized by small sedimentary thicknesses (< 2 km) over a thin crust (ca. 15 km) where a distinct patch of high-velocity lower crust occurs (Eakin et al., 2014; Lester et al., 2014; Liu et al., 2023, 2021; Yeh et al., 2010). This high-velocity layer, identified in refraction profiles throughout the area, ranges between 2-4 km thick and is interpreted as related to the underplating beneath the passive margin after the cessation of seafloor spreading (Pin et al., 2001; Wei et al., 2011; Zhao et al., 2010). Two seamounts were dredged and dated in the SH, recording basalts with three discrete ages: late Jurassic (154.1 ±1.8 Ma; whole-rock Ar-Ar), late Cretaceous (93.2 ±5 Ma; whole-rock Ar-Ar) and early Miocene (21 ±0.2 Ma; whole-rock Ar-Ar) (Wang et al., 2012a; Xu et al., 2022) (Figure 1). Despite these basalts samples leading toward a magmatic nature of the SH crust, there is still no consensus about the crust composition of the region. The SH has been already interpreted as composed of a thin continental crust interspersed with magmatic additions (Bautista et al., 2001; Fan et al., 2017; Lester et al., 2014; Liu et al., 2023, 2021; Sibuet et al., 2016), part of the Philippines Plate oceanic crust (Hsu et al., 2004), relicts of a thick Mesozoic oceanic crust (Reed, 1995; Sibuet et al., 2016; Yeh et al., 2012, 2010), and even a Mesozoic oceanic plateau (Xu et al., 2022).

3. DATA AND METHODS

3.1. Seismic reflection data

87 open-access seismic reflection profiles from 8 surveys (covering over 15000 km) were used in this study. Of those lines, 3 are from survey RC2006 (Hayes, 2011), 23 from RC2612 (Hayes, 2015), 5 from V3608 (Talwani, 2015), 8 from V3613 (Hayes, 2011b), 9 from V3614 (Leyden, 2015), 7 from EW9509 (Reed, 1995), 22 from MGL0905 (C.-S. Liu et al., 2018), and 10 from MGL0908 (McIntosh et al., 2017) (Figure 2a). For a complete list of the open-access reflection seismic lines used in this study, the reader is referred to Supplementary Table S1. The parameters of each survey are given in Supplementary Table S2. Seismic polarity follows the American system.

For this work, we mapped the seabed, top acoustic basement (Tg), top of the high-velocity lower crust (HVLC), and seismic Moho. Seismic horizons were subsequently interpolated using the convergent interpolation method with a gridding spacing of 1957 x 1957 m. The identification of the igneous intrusions in seismic reflection data follows the criteria described in Jamtveit et al. (2004), Planke et al. (2005), Schofield et al. (2012), and Magee et al. (2013, 2015, 2018).

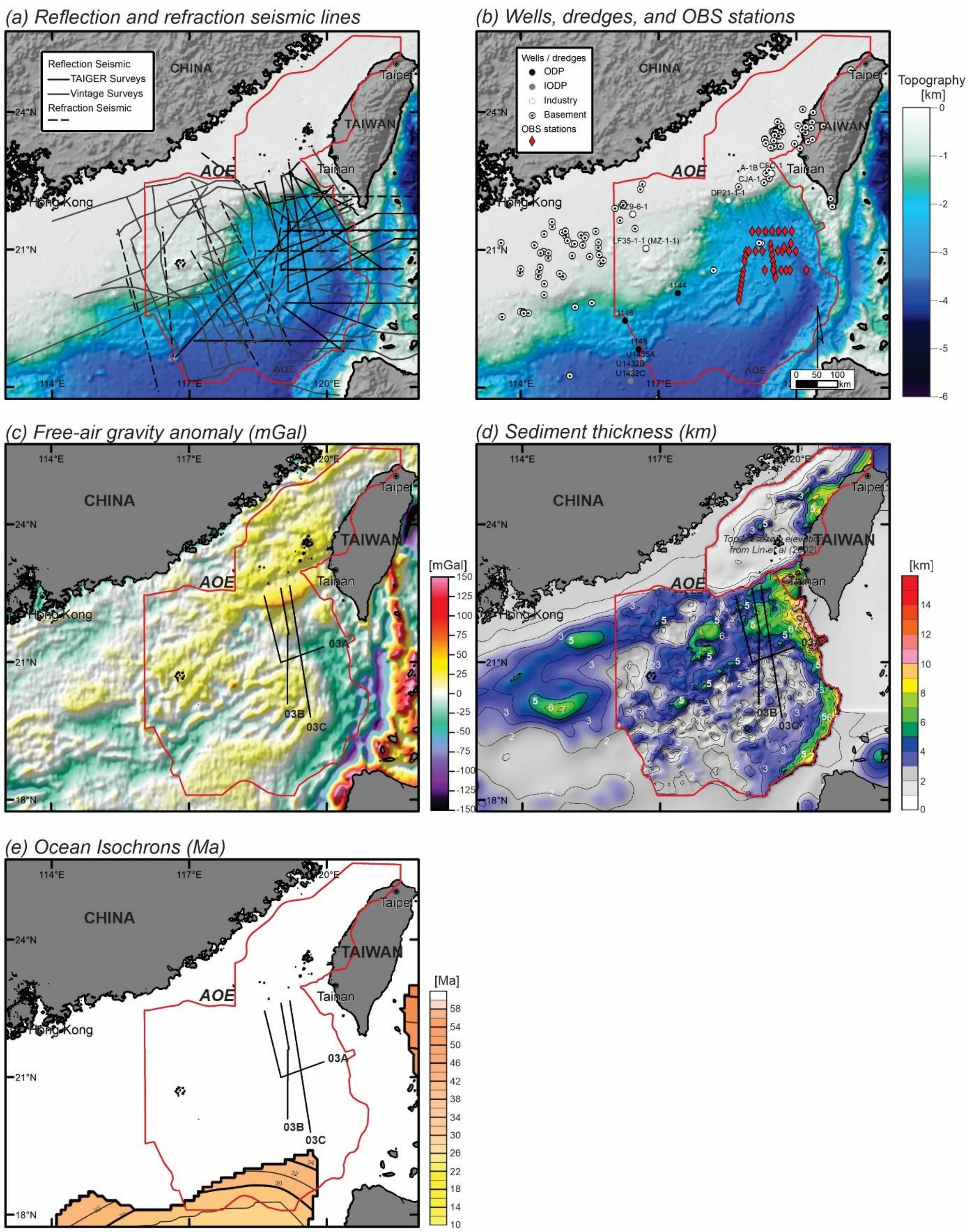

Figure 2. Data used in this study. (a) 2D data used in this study, such as reflection and refraction seismic. (b) 1D data used in this study, such as well logs, location of drilled basement rocks, and OBS stations. (c) Free-air satellite-derived gravity anomaly data (Sandwell et al., 2014). (d) Sediment thickness (m). Data outside the area of exploration is from public domain data (Divins, 2003). Contour lines are between 1 km each. (e) Ocean isochrons (Barckhausen and Roeser, 2004; Barckhausen et al., 2014). Contour lines are between 2 Ma each. AOE – area of exploration.

3.2. Seismic refraction data and depth conversion

We compiled the velocity information from 12 seismic refraction profiles to build the velocity volume we used to depth convert the seismic horizons picked in the time domain (Figure 2a). These profiles are the OBS1993 (Yeh et al., 1998), line 29-33 (McIntosh et al., 2005), OBS2001 (Wang et al., 2006), OBS2006-3 (Wei et al., 2011), MGL0905-27 (Lester et al., 2013), OBST1 and OBST2 (Eakin et al., 2014), OBST3 (Lester et al., 2014), OBS2012 (Wan et al., 2017), OBS2015-2 (S. Liu et al., 2018), OBS2016-2 (Wan et al., 2019), OBS2019 (Liu et al., 2021) (Figure 2a). Velocities depth profiles from the SH region were extracted from MGL0905 (stations 2 and 3), OBST1 (stations 4, 5, 6, 10), OBST2 (stations 1 to 7), OBST3 (stations 8, 9, 10, and 11), and OBS2015 (stations 7 and 8) to build a velocity envelope representative of the SH basement. (Figure 2a)

The velocity volume was made using a gridding space of 958.3 x 958.3 km and two bounding surfaces: seabed and base Cenozoic (Tg). A seawater velocity of 1500 km/s was used. Below the seabed, the vertical resolution was set as 200 m, and layering followed the base surface (Tg). Sediment velocities (from the seabed to Tg) were interpolated using a moving average in an isotropic medium. The results were compared to a set of depth-converted seismic profiles available from the TAIGER survey (C.-S. Liu et al., 2018). Depth-converted seismic interpretation of the seabed was combined with open-source topographic and bathymetric data (Tozer et al., 2019). Depth converted Tg (m) as interpreted in this study was merged with a depth to the base syn-rift grid compiled by Lin et al. (2003) in the proximal margin (Figure 2d).

3.3. Wells, dredges, and other data

Different geological data sets are compiled in this work. Wells are from IODP/ODP surveys (Li et al., 2015; Wang et al., 2000), and from industry made available through publications. Wells that reached Mesozoic sediments are from Lu *et al.* (2014) and Fan *et al.* (2022) and references therein (Figure 2b). Information on granitoids sampled from wells is from Shi *et al.* (2011), Xu *et al.* (2016), Li *et al.* (2018), and references therein (Figure 2b). Wells that reached Tertiary volcanic intervals in Taiwan Strait and Taiwan are from Wang *et al.* (2012a) (Figure 2b). Dredges of volcanic seamounts were later discretized based on their age being either Cenozoic (Fan et al., 2017; Zhang et al., 2016; Zhong et al., 2018) or Mesozoic (Xu et al., 2022). We also integrated basement data available from onshore Taiwan (Tian et al., 2019) and Penghu Islands (Figure 2b) (Chen et al., 2010; Juang and Chen, 1992).

Structures are compiled from different publications (Figure 1): (i) PRMB (Lei et al., 2018; Xie et al., 2019), (ii) Nanjihtao, Taihsi, and Penghu basins (Lin et al., 2003), (iii) Tainan Basin (*sensu strictu)* (Lin et al., 2003; Huang et al., 2012). These local structures were integrated with regional maps from Pubellier et al. (2016) and Sibuet et al. (2016). Granitic bodies are according to Pubellier et al. (2016). Volcanic seamounts are based on Sun et al. (2010), Lei et al. (2018), and this work. Interpreted magnetochrons of the SCS are from Briais et al. (1993) (Figure 1A and C).

3.4. Gravity inversion

We use a gravity inversion scheme to determine Moho depth and crustal thickness (Alvey et al., 2008; Chappell and Kusznir, 2008; Gozzard et al., 2019; Greenhalgh and Kusznir, 2007). The technique uses satellite-derived free-air gravity anomaly data (Sandwell et al., 2014), bathymetry (Tozer et al., 2019), sediment thickness, and ocean age (Barckhausen and Roeser, 2004; Barckhausen et al., 2014) to calculate mantle residual gravity anomaly. Sediment thickness is compiled from different sources. In our area of interest, sediment thickness is defined between the seafloor and the depth-converted top basement (Tg) (Figure 2d) (Lin et al., 2003 and this work). Outside the area of exploration, we use the global compilation of sediment thickness (Divins 2003) as used by Gozzard et al. (2019). Despite the different resolutions, the two data sources merge well (Figure 2d). The gravity anomaly inversion is carried out in the 3D spectral domain following the scheme of Parker (1972) to give 3D Moho geometry. The inversion for Moho depth invokes Smith's theorem (Smith, 1961) which provides a unique solution for the assumptions made. We use a constant density for the crust of 2850 kg.m^{-3} and for the mantle of 3300 kg.m^{-3}.The determination of an absolute Moho depth requires a reference datum referred to as the reference Moho depth (Kusznir et al., 2018). This geophysical/geodetic parameter varies globally, controlled by the long wavelength components of the Earth's gravity field (Cowie et al., 2015). A reference Moho depth of 40 km was previously calibrated at the scale of the whole SCS (Gozzard et al., 2019). Calibrations against refraction data (ESP-1 from Nissen et al., 1995) in our area of interest suggest that close to the subduction zone the reference Moho depth slightly increases to 41 km.

The gravity inversion method includes both a lithosphere thermal gravity anomaly correction and a prediction of magmatic addition (Alvey et al., 2008; Chappell and Kusznir, 2008; Greenhalgh and Kusznir, 2007; Kusznir et al., 2018). The lithosphere thermal gravity anomaly correction is dependent on the assumed rifting/break-up age. Rifting in the SCS has previously been attributed to several ages that range between two endmembers: (i) the opening of the Proto SCS (Dycoco et al., 2021 and references therein), (ii) the opening of the SCS (Li et al., 2014 and references therein). Ophiolite remnants from southern Palawan suggest that the Proto SCS opened in the Late Cretaceous (parametrized with a rifting age of 100 Ma) (Dycoco et al., 2021). Conversely, the end of rifting and onset of seafloor spreading in the SCS is based on the age interpretation of the C11 magnetic anomaly (Briais et al., 1993), parametrized as ca. 33 Ma (Li et al., 2014). As the magnitude of the gravity anomaly decreases with time, these end-member rifting/breakup ages provide different Moho depth and crustal thickness results that can be compared to seismic data. The prediction of magmatic addition uses a parametrization of the decompression melt model of White and McKenzie (1989). We assume a maximum decompression melt volume of 7 km consistent with the observation of normal thickness oceanic crust (Li et al. 2014).

3.5. Joint inversion of seismic and gravity data

The gravity inversion technique described above assumes a fixed crustal density. In order to investigate lateral crustal density variations along the profiles, we use a joint inversion to compare the Moho determined from gravity inversion with that interpreted from time-migrated seismic reflection sections (Cowie et al., 2017; Harkin et al., 2019; Nirrengarten et al., 2020). The joint inversion method determines the lateral variation of crustal seismic velocities and densities needed for the gravity-inverted Moho to match the interpreted seismic Moho in the time domain. The Moho from gravity inversion is taken into the time domain using the empirical relationship of Birch (1964) linking seismic velocity (Vp in $km.s^{-1}$) with density (ρ in $kg.m^{-3}$). The constant 2850 $kg.m^{-3}$ crustal density considered in the gravity inversion scheme corresponds to a seismic velocity of 6.72 $km.s^{-1}$. Iterative adjustments of both crustal densities and seismic velocities are made to provide a fit of the gravity Moho (in time) with the interpreted seismic Moho in TWT. The comparison of gravity and seismic Moho is made in the time domain to avoid uncertainties in the depth conversion of seismic reflection data. This joint inversion technique requires seismic reflection profiles that image seismic Moho. Seismic lines that meet this criterion were chosen for this study (Figure 2c, d, and e). We have applied the joint inversion technique to gravity inversion results using end member break-up ages of 33 Ma and 100 Ma.

4. SEISMIC OBSERVATIONS

4.1. Interpretation approach and definition of first-order seismic horizons

We identified, interpreted, and mapped first-order seismic horizons of the NE SCS margin, which are from shallowest to deepest: the seafloor, Top acoustic basement (Tg), top high-velocity lower crust (HVLC), and Seismic Moho (Figure 3a to c).

The seafloor is the first high-impedance contrast in our reflection seismic lines (Figure 3). The seafloor is generally flat over the continental shelf. The slope area is characterized by a high topographical gradient where submarine canyons, channels, and gullies occur (Figure 3). In the abyssal plain, the seafloor is relatively flat, despite the local occurrence of submarine channels and seamounts (Figure 3). These seamounts are regions where the top basement locally crops out, probably representing volcanoes. Some of these seamounts were already dredged, sampling Mesozoic and Miocene basalts (i.e., Beipo and Puyuan-Formosa seamounts) (Wang et al., 2012a; Xu et al., 2022) (Figure 1 and Figure 3a).

The top basement (Tg) is mapped at the base of the Cenozoic infill, corresponding to syn-rift (SRS and SH) or post-rift sequences (SH). Therefore, the top basement corresponds to a diachronous surface, on top of which significant sediment thickness variations are observed (Figure 2d).

The Tg interface in the Tainan Basin does not always correspond to a clear reflector. Instead, it is mapped where a change from parallel and well-stratified reflectors (interpreted as representing Cenozoic sediments) to undulated and discontinuous seismic facies occurs (Figure 3). This interface is usually observed close to the 4 s (TWT) (Figure 3a) and 5 km (depth) (Figure 3b and c). Tg is often offset by counter-regional normal faults delimiting rift basins (Figure 3a), which offsets that can surpass 1 s (TWT) (Figure 4a) and 2 km (depth) take place (Figure 4b and c). The undulated and discontinuous seismic facies underneath Tg consist of Mesozoic pre-rift strata, an observation supported by drilling results (Figure 2b) (Gong et al., 1997; Lu et al., 2014; Taylor and Hayes, 1983; Wang et al., 2012a; Xi et al., 2005; Zhou, 2002) and refraction seismic (Lester and McIntosh, 2012; Liu et al., 2021).

From the Tainan Basin to the SRS axis, a gradual deepening of Tg is observed over ca. 70 km (Figure 4). Tg passes from values as low as 2.5 s (TWT) (4 km deep) in the Central High to ca. 8 s (TWT) (more than 9 km deep) in the SRS (Figure 4). In this rift system, the Tg horizon is mapped along a high amplitude reflector, below which the acoustic basement shows chaotic, hummocky, and semi-parallel seismic facies. There, Tg is reached after 5 s (TWT) and 6 km (depth), being frequently offset by many regional and counter-regional normal faults that can surpass 1 s (TWT) and 1 km (depth) (Figure 4b and c). Adjacent to the rift axis and below Tg, parallel reflectors with synform (Figure 3a) and antiform (Figure 3b) geometries are observed. These pre-rift reflectors fit with the seismic region that has been interpreted, based on Vp from refraction seismic, as Mesozoic sedimentary sequences (Liu et al., 2023, 2021).

Tg rises towards the SH (Figure 3) to elevations as low as 6 s (TWT) and 7 km (depth) (Figure 4). This sudden offset of Tg is interpreted to be controlled by a system of major normal faults, here referred to as the Boundary Fault Zone (BFZ) (Figure 3a to c). In the SH, Tg is mapped along a rather continuous and high-amplitude reflector. Top basement topography is either flat or irregular, where seamounts and buried mounts occur (Figure 3b, and c). Pre-rift sedimentary reflectors seem absent; however, they might sparsely occur in zones where stratiform seismofacies are observed (Figure 3). Faulting is sparse and, when present, characterized by low offsets (Figure 3b and c; Southern High).

The top of the high-velocity lower crust (i.e., HVLC, velocities between 6.9-7.5 km/s), recognized in refraction seismic data in the Tainan Basin (Zhao et al., 2010) and the SH (Eakin et al., 2014; Lester et al., 2014; Liu et al., 2023, 2021). This HVLC horizon is mapped in seismic reflection data on top of a set of laterally continuous, high-amplitude reflectors (Figure 3a and c) (see also Lester et al., 2014). The top of the HVLC surface pinches out on the interpreted seismic Moho towards the axis of the SRS (Figure 3a and c), where no HVLC appears on refraction seismic data (Liu et al., 2023, 2021).

The seismic Moho is picked at the base of a band of high-amplitude, discontinuous flat reflectors lying around 10s (TWT) in the Tainan Basin. Seismic Moho interpretation is less constrained in the slope area due to the absence of clear high-amplitude reflectors deep in the crust (Figure 3b-c). Towards the SRS, seismic Moho reflection corresponds to a clear high-amplitude reflector on some profiles (Figure 3a). Seismic Moho rises to 7.5-8 s (TWT) at the rift axis, where the crust is as thin as 0.3 to 0.8 s (TWT) (Figure 3). Seismic Moho progressively deepens down to 9.5-10 s (TWT) at the location of the Boundary Fault Zone (Figure 3a-c). In the SH, it rises to values from 9 to 8 s (TWT) from ca. 30 km (Figure 3c) to 70 km of distance (Figure 3c). In the SH, seismic Moho is mapped along discontinuous high-amplitude reflectors locally located underneath transparent seismic facies within the HVLC (Figure 3b-c).

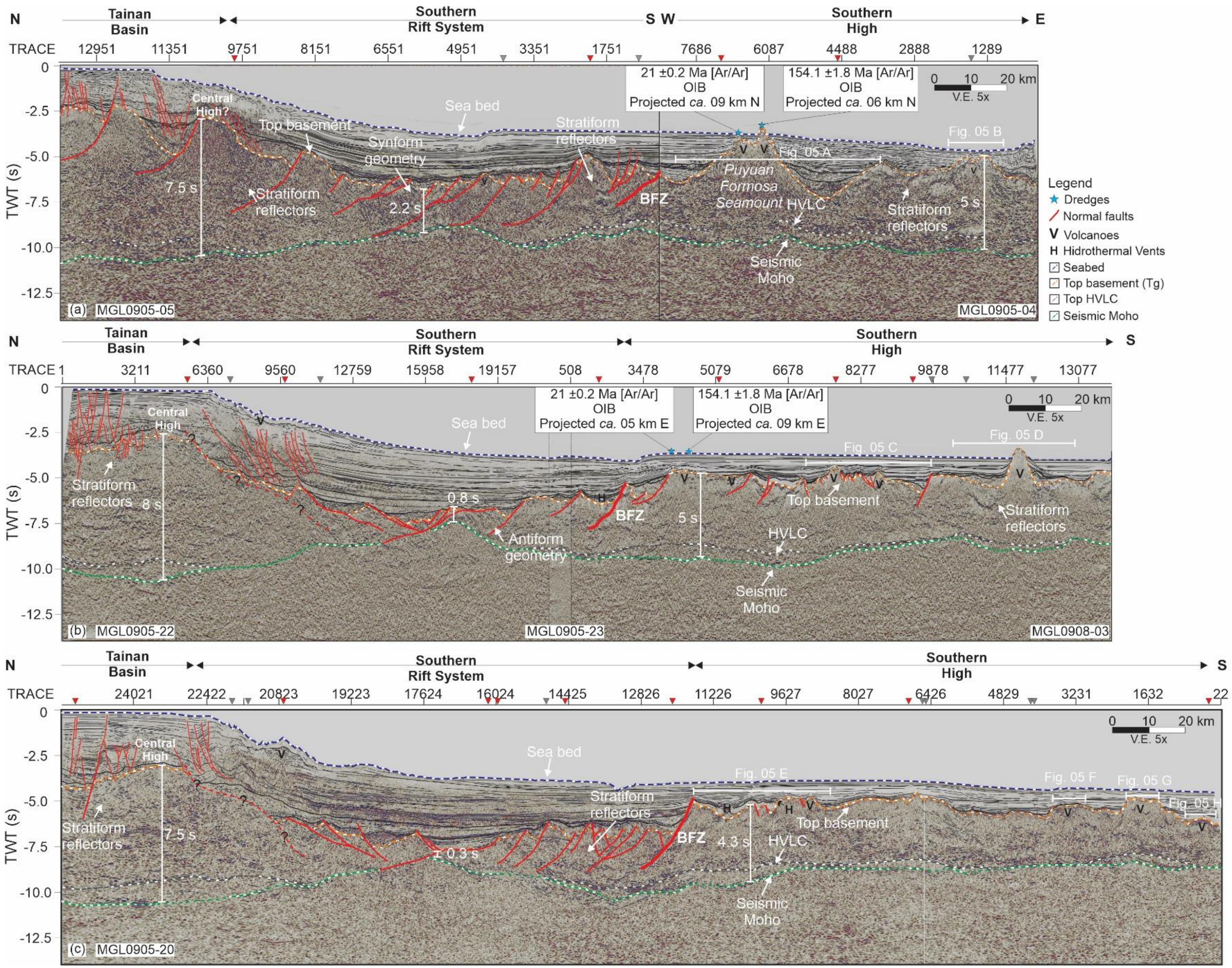

N
Tainan Basin
Southern Rift System
S W
Southern High
E
TRACE
12951
11351
9751
8151
6551
4951
3351
1751
7686
6087
4488
2888
1289
21 ±0.2 Ma [Ar/Ar]
OIB
Projected ca. 09 km N
154.1 ±1.8 Ma [Ar/Ar]
OIB
Projected ca. 06 km N
0 10 20 km
V.E. 5x
Central High?
Top basement
Sea bed
Synform geometry
Stratiform reflectors
Fig. 05 B
Fig. 05 A
7.5 s
2.2 s
BFZ
Puyuan Formosa Seamount
HVLC
5 s
Seismic Moho
TWT (s)
(a) MGL0905-05
MGL0905-04
Legend
Dredges
Normal faults
V Volcanoes
H Hidrothermal Vents
Seabed
Top basement (Tg)
Top HVLC
Seismic Moho
N
Tainan Basin
Southern Rift System
Southern High
S
TRACE 1
3211
6360
9560
12759
15958
19157
508
3478
5079
6678
8277
9878
11477
13077
21 ±0.2 Ma [Ar/Ar]
OIB
Projected ca. 05 km E
154.1 ±1.8 Ma [Ar/Ar]
OIB
Projected ca. 09 km E
Central High
Sea bed
Fig. 05 C
Fig. 05 D
Stratiform reflectors
8 s
0.8 s
BFZ
5 s
Top basement
Antiform geometry
HVLC
Seismic Moho
(b) MGL0905-22
MGL0905-23
MGL0908-03
N
Tainan Basin
Southern Rift System
Southern High
S
TRACE
24021
22422
20823
19223
17624
16024
14425
12826
11226
9627
8027
6426
4829
3231
1632
22
Central High
Sea bed
Fig. 05 E
Fig. 05 F
Fig. 05 G
Fig. 05 H
Stratiform reflectors
7.5 s
0.3 s
BFZ
4.3 s
Top basement
HVLC
Seismic Moho
(c) MGL0905-20
0
-2.5
-5.0
-7.5
-10.0
-12.5

372

Figure 3. Selection of reflection composite seismic lines illustrating the key structural elements of the NE SCS, such as the line drawing, and horizons used in this study. To check the location of the lines, the reader is referred to Figure 2E (a) Composite section made with MGL0905-05 (N-S dip-oriented) and MGL0905-04 (W-E; strike-oriented). (b) Composite section made with MGL0905-22 (N-S dip-oriented), MGL0905-23(E-W; strike-oriented), and MGL0908-03 (N-S; dip-oriented). (c) Seismic line MGL0905-20 (N-S; dip-oriented). BFZ – Boundary fault zone. HVLC – Top of High-velocity lower crust.

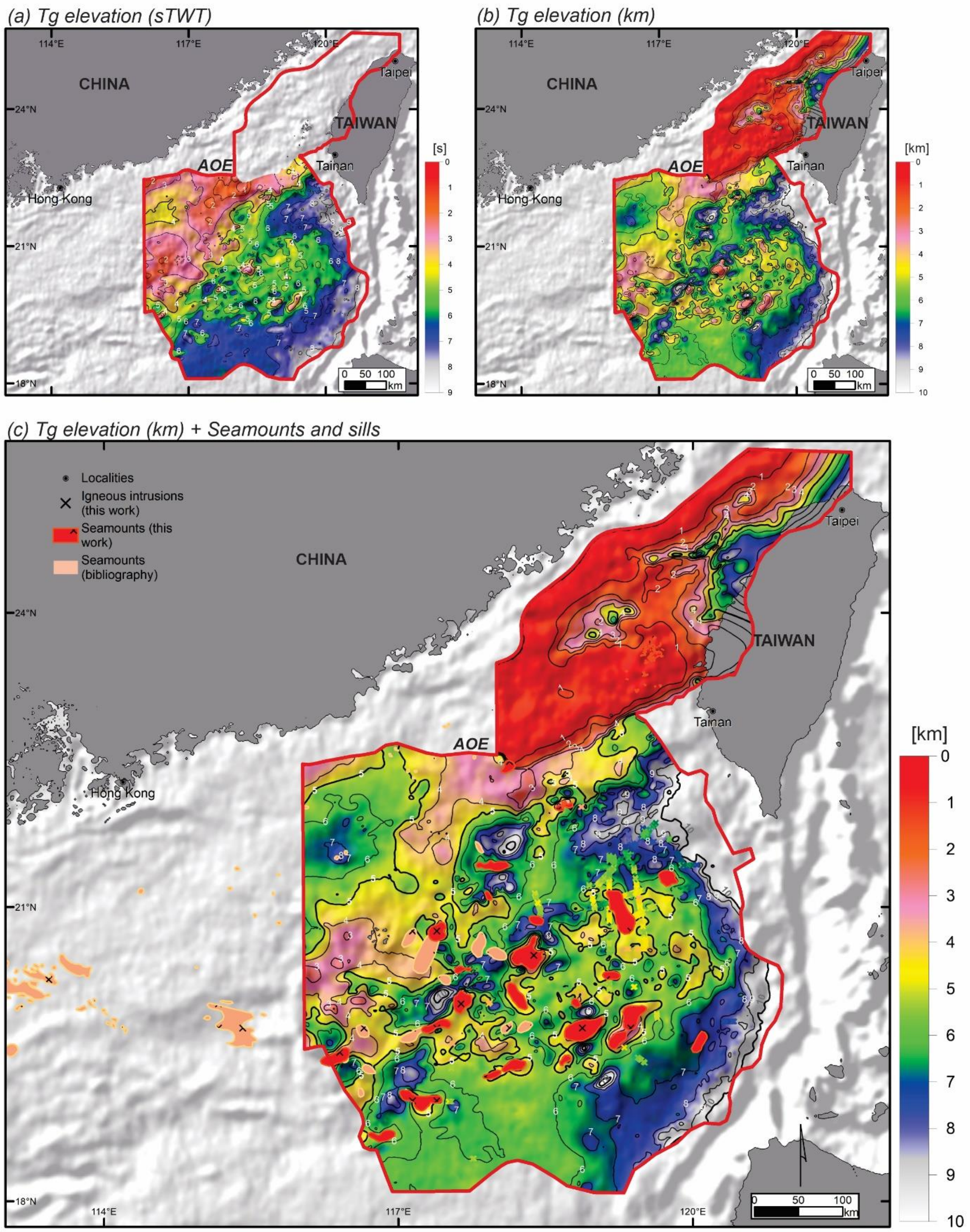

Figure 4. Elevation maps to reach the top basement (Tg) in (a) time (s TWT), and (b) depth (km). (c) Tg elevation (km) integrated with seamounts (Sun et al., 2010; Lei et al., 2018, and this work) and mapped igneous intrusions (e.g., sills; this work). AOE- area of exploration.

4.2. Identification and distribution of magmatic additions

Several volcanic features and igneous intrusions have possibly been identified in the basement, based on the geometry of reflectors and seismic facies (Jamtveit et al., 2004;

Magee et al., 2018, 2015, 2013; Planke et al., 2017, 2005; Schofield et al., 2012; Xu and Haq, 2022), and available dredges (Wang et al., 2012a; Xu et al., 2022).

In the SH, layer-parallel high amplitudes and saucer-shaped reflectors are common intruding older sequences of the Cenozoic and/or shallowest portions of the basement (Figure 5A, C, D, E, G). Those two seismofacies are usually attributed to the acoustic response to sheet intrusions such as sills and magma fingers (Magee et al., 2015; Planke et al., 2005). The sills intruding the Cenozoic sequences are commonly interpreted not only in the SH (around 4 to 5 km deep) but also in the southern part of the SRS (around 4 to 7 km deep) (Figure 3c and Figure 4c).

These magmatic additions are laterally related to several features. Eye- (Figure 5E), dome-, and crater-shaped morphologies are observed (Figure 5F). Such features are commonly related to cones and sills sometimes associated with hydrothermal vent complexes (Jamtveit et al., 2004; Planke et al., 2005). Seamounts characterized by abrupt changes of top basement topography (e.g. Figure 5A, C) show granular to chaotic seismofacies and velocity pull-ups as well as the absence of deep reflectors (i.e., HVLC and seismic Moho) (Figure 5A, and D). The pull-ups indicate velocity contrasts between the seamount medium (denser) and its surroundings (lighter) (Magee et al., 2013). This assemblage observed in the outcropping or buried seamounts is interpreted as volcanoes, an assumption validated by dredging in the area (i.e., Beipo and Puyuan-Formosa seamounts) (Wang et al., 2012a; Xu et al., 2022). A majority of the mapped magmatic seamounts have no geometry that suggests erosional processes (Figure 5D). Nonetheless, some of them (e.g., Puyuan-Formosa) (Figure 4a) (Wang et al., 2012a; Xu et al., 2022), have a finger-like morphology, which may indicate a long-lasting exposition to erosion (Figure 5A). In general, these volcanoes are mostly present throughout the SH. They have no clear directional trend and vary from patches as small as 5 km to more than 30 km wide (Figure 4c). In the Tainan Basin and SRS, some smaller volcanic patches also occur with a general ENE-WSW orientation (Figure 4c). Sometimes, granular with high frequencies internal reflectors occur in the Tg interface, which is common in inner flow seismofacies as the acoustic response to lava flows (Planke et al., 2017) (Figure 5H).

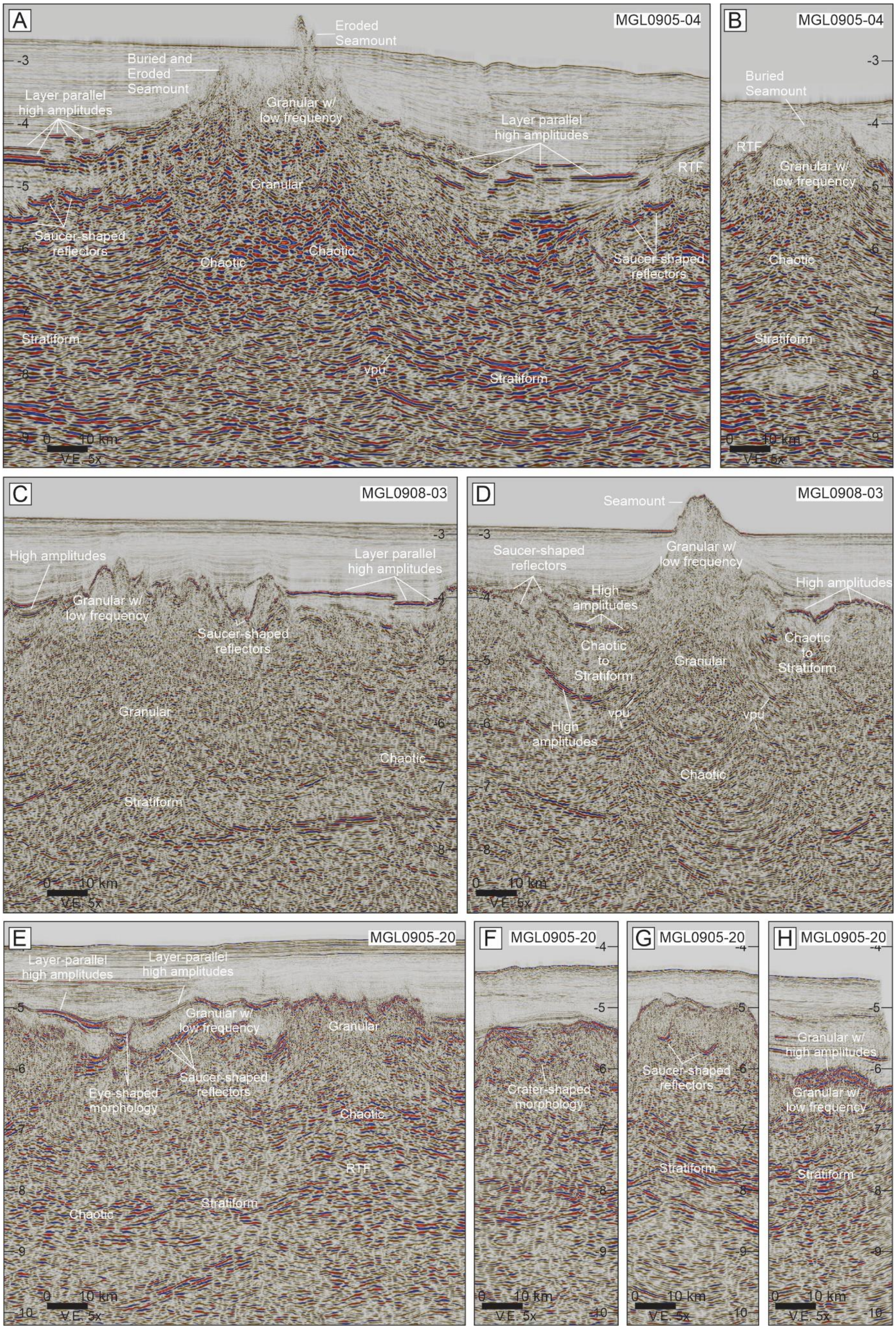

A
MGL0905-04
Eroded Seamount
Buried and Eroded Seamount
Layer parallel high amplitudes
Granular w/ low frequency
Layer parallel high amplitudes
RTF
Granular
Saucer-shaped reflectors
Chaotic
Chaotic
Saucer-shaped reflectors
Stratiform
vpu
Stratiform
0 10 km
V.E. 5x
B
MGL0905-04
Buried Seamount
RTF
Granular w/ low frequency
Chaotic
Stratiform
0 10 km
V.E. 5x
C
MGL0908-03
High amplitudes
Layer parallel high amplitudes
Granular w/ low frequency
Saucer-shaped reflectors
Granular
Chaotic
Stratiform
0 10 km
V.E. 5x
D
MGL0908-03
Seamount
Saucer-shaped reflectors
Granular w/ low frequency
High amplitudes
High amplitudes
Chaotic to Stratiform
Granular
Chaotic to Stratiform
vpu
vpu
High amplitudes
Chaotic
0 10 km
V.E. 5x
E
MGL0905-20
Layer-parallel high amplitudes
Layer-parallel high amplitudes
Granular w/ low frequency
Granular
Eye-shaped morphology
Saucer-shaped reflectors
Chaotic
RTF
Stratiform
Chaotic
0 10 km
V.E. 5x
F
MGL0905-20
Crater-shaped morphology
0 10 km
V.E. 5x
G
MGL0905-20
Saucer-shaped reflectors
Stratiform
0 10 km
V.E. 5x
H
MGL0905-20
Granular w/ high amplitudes
Granular w/ low frequency
Stratiform
0 10 km
V.E. 5x

Figure 5. Crustal seismic expression of some transects from the NE SCS Southern High. A – Puyuan-Formosa Eroded Seamount, composed of Jurassic and Miocene basalts (Wang et al., 2012a; Xu et al., 2022) laterally related to sills. B – Concave buried volcanic seamount laterally related to sills. C – Buried volcanic seamount complex made of several small-scale concave-shaped reflectors. Laterally, hydrothermal vent complexes and sills can occur. D – Volcanic seamount with concave-shaped morphology. E – Hydrothermal vent complex composed of eye-shaped and layer-parallel high amplitude morphologies. F – Volcanic crater complex in a buried plateau. G – Plateau morphology intruded by sills. H – Inner flow close to the sediment-crust boundary. vpu – velocity pull-up.

4.3. Characteristics of structural domains: synthesis

The interpretation of the seafloor, top basement, top of the HVLC, and seismic Moho enables the mapping of the sediment and crustal thickness evolution in the NE SCS margin segment. Variations of sediment and crustal thicknesses and the mapping of magmatic seamounts are used to define different structural domains:

The proximal margin occurs north of AFZ (Figure 1A). This domain is characterized by a <3.5 s (TWT) (<6 km; Figure 2d) thick Cenozoic succession, where isolated Cenozoic rift basins from the *Northern Rift System* occur (i.e., Penghu, Nanjihtao, Taihsi), overlying a relatively weakly thinned crust (~7.5-8 s TWT thick, Figure 4d) (Lin et al., 2003). Cenozoic magmatism is common and well-known in areas such as Penghu Island, Penghu High, Taiwan Strait (Chung et al., 1994; Juang and Chen, 1992; Wang et al., 2012a), and onshore Taiwan (Chung et al., 1994; Smith and Lewis, 2007). Mesozoic and Paleozoic pre-rift strata are present below Tg, inference validated by subsurface data (Figure 3).

The Tainan Basin occurs between the AFZ and the Central High. It is characterized by a 3 to 4 s (TWT) (3 to 5 km; Figure 2d) thick Cenozoic succession. The seismic Moho signal tends to be clear and around 10 s (TWT). The top of the HVLC signal is observed and pinches out toward the south. Mesozoic pre-rift strata are likely locally present below Tg, as sampled in several boreholes (Figure 3).

The *Southern Rift System* (SRS) occurs from the south of the Central High to the BFZ (Figure 1A). This domain is characterized by thick Cenozoic sedimentary succession (<7.5 s TWT) (<6 km; Figure 2d). Thin syn-rift strata are widely present (around 0.5 s TWT), overlying a hyper-thinned crust locally less than 0.3 s (TWT) thick close to the rift axis. The HVLC is absent under the SRS. Mesozoic pre-rift strata are possibly present below Tg, showing folded geometries, but have never been drilled at this location (Figure 3). Magmatic intrusions such as sills, dykes, and magma fingers are possibly present in great numbers throughout the southern part of the rift axis (Figure 5).

The *Southern High* (SH) occurs from the south of the boundary fault zone to the oceanic domain This domain is characterized by a thicker crust (3 to 5 s TWT), compared to the SRS, where thin Cenozoic sedimentary succession (<2 s TWT; 2 to 3 km) tend to occur.

Magmatic additions are frequently observed forming seamounts, intrusions, and flows (Figure 3c). Some of them are clearly of post-rift age (Figure 5A). Seismic facies do not support the interpretation of Mesozoic strata to the south of the Boundary Fault Zone. However, their presence below magmatic addition cannot be excluded (Lester et al., 2014). The presence of a 3-5 km thick HVLC (6.7 to 7.3 km/s; Lester et al., 2014) has been interpreted as magmatic underplating or lower crustal intrusions possibly of post-rift age (Lester et al., 2014; Liu et al., 2021).

4.4. Velocity envelopes of the Southern High

The velocity structure below the top basement is commonly represented as a velocity envelope that is used to test oceanic or continental crustal type (Figure 6). Velocities of the upper part of the SH basement range from ca. 4.3 to 5.5 km/s and slowly increase with depth up to ca. 6–7 km/s at 5 km depth. A net shift towards higher velocities (ca. 6.7–7.8 km/s) is observed below 10 km depth and down to 15 km depth (Figure 6). This shift corresponds to the ca. 3 to 5 km high-velocity lower crust (ca. 6.9–7.5 km/s) (Lester et al., 2014; Liu et al., 2021).

We compared the velocity envelope of the SH with the compilation of Pacific oceanic crust thicknesses shown in White et al. (1992). We also included in our comparison, the velocity profile for the thick (i.e., 12.5 km thick) oceanic crust compiled by Mutter & Mutter (1993) (Figure 6a). The crust of the SH is locally up to 15 km thick (Figure 6) and is hence thicker than the global oceanic crust average (i.e., 7.1 ±0.8 km) (White et al., 1992) and does not correspond to a typical oceanic crust. The comparison with the thick oceanic crust velocity profile of Mutter & Mutter (1993) shows a better fit, although velocities tend to be slightly slower (<0.5 km/s) between 3 to 10 km depth (Figure 6a).

The velocity structure of the SH was also compared to that compiled for the thin continental crust (Prada et al., 2015) (Figure 6b). It is noteworthy that the SH crust is thicker than the data collected by Prada et al. (2015). The velocity structure of the SH shows a trend similar to that of thinned continental crust down to 10 km thick, although lower velocities are also commonly compiled for the area. However, no HVLC is observed in the thin continental crust compilation of Prada et al., (2015) (Figure 6b).

Because of the similar velocity range between continental and oceanic crustal rocks, velocity envelopes determined from wide-angle seismic data cannot easily be used to discriminate unambiguously the crustal type (Karner et al., 2022). Although we cannot conclude on the crustal type of the SH at this point, we note that its velocity structure is similar to that of the distal SCS margin located to the west (Figure 6c) (Nissen et al., 1995; Pin et al., 2001; Wang et al., 2006) as previously pointed out by Lester et al, (2014). There, the distal SCS rifted margin is interpreted to be of continental origin, locally intruded by magmatic additions (Bautista et al., 2001; Fan et al., 2017; Lester et al., 2014; Liu et al., 2023, 2021; Sibuet et al., 2016).

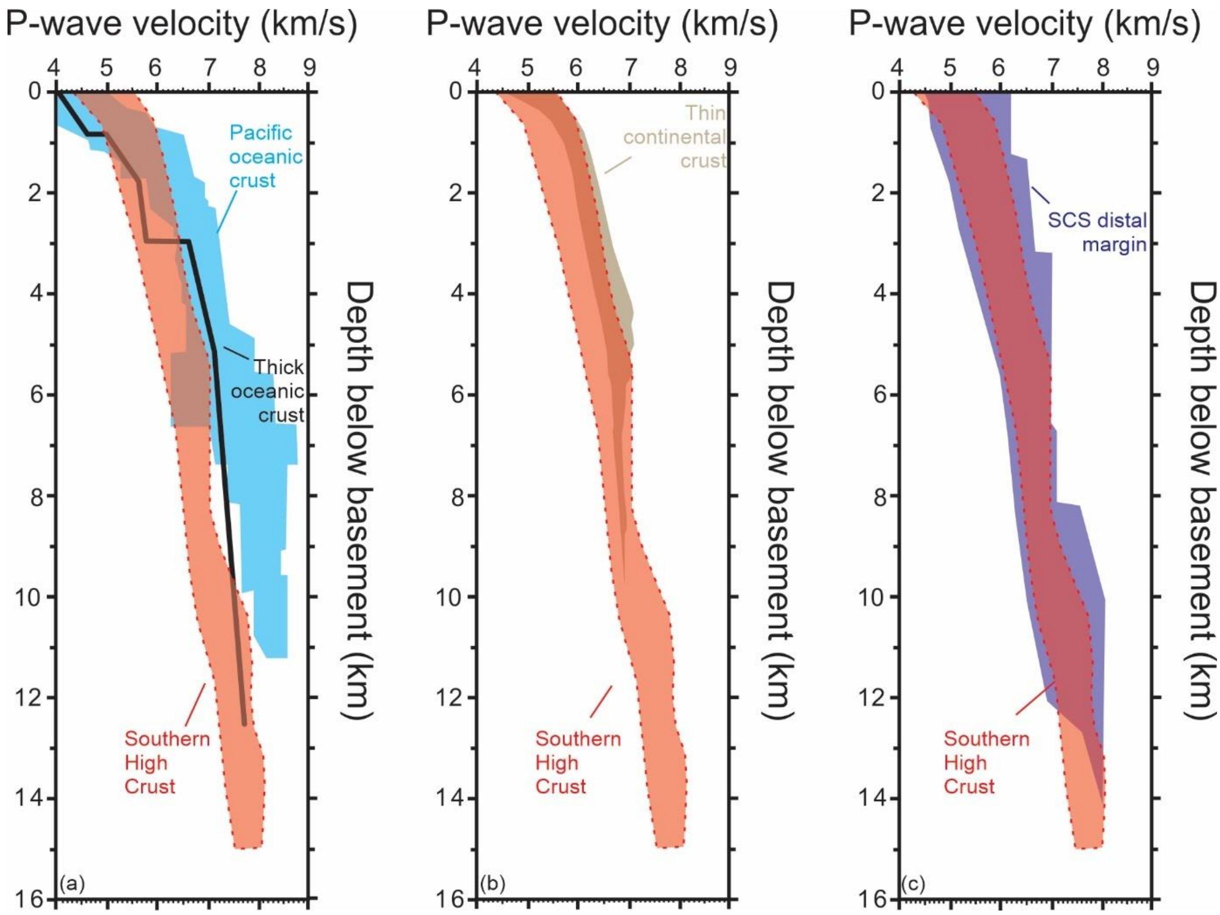

Figure 6. Velocity envelopes compiled for the Southern High compared to (a) Pacific-type oceanic crust (White et al., 1992) and 12.5 km thick oceanic crust velocity profile (Mutter and Mutter, 1993); (b) thin continental crust (Prada et al., 2015); (c) Western SCS distal margin velocity envelope (Lester et al., 2014).

5. GRAVITY INVERSION AND JOINT SEISMIC-GRAVITY INVERSION

5.1 Gravity inversion

Crustal thickness maps produced by gravity inversion are shown in Figure 7. As mentioned earlier, the reference Moho depth of the gravity inversion results was calibrated against refraction data over unambiguous oceanic crust (ESP 1 in Nissen et al., 1995) formed subsequently to early Oligocene breakup (Li et al., 2014). The formation age of the SRS and the SH is, however, less constrained. Cenozoic and Mesozoic ages have been suggested to correspond to either the opening of the South China Sea (Briais et al., 1993; Li et al., 2014) or the Proto-South China Sea (Dycoco et al., 2021 and references therein). The elapsed time for lithosphere thermal re-equilibration directly impacts the lithosphere thermal gravity anomaly correction and hence the gravity-derived Moho depth and crustal thickness. We have tested the sensitivity of the gravity-derived Moho depth and crustal thickness to end-member formation ages 33 Ma and 100 Ma for the SRS and the SH (Figure 7). Crustal thicknesses assuming an age of 33 Ma for lithosphere thermal re-equilibration are shown in Figure 7a. Inside our area of interest, gravity-derived crustal thickness is determined using our sediment thickness compilation (Figure 2b); outside of it, public-domain sediments are used (Divins et al. 2003). Different crustal domains can be distinguished in Figure 7. Over the continental shelf, west of Taiwan, crustal thickness is predicted to be 30 km thick or slightly thicker, except at the location of the Penghu (<30 km), Nanjihtao (<25 km), and Taihsi (<20 km) depocenters (Figure 7a). Note that the crustal thickness over the continental shelf could be slightly overestimated if thick Mesozoic sedimentary sequences are present below the interpreted top basement (i.e., Top of Mesozoic of Lin et al., 2003). Over the present-day continental shelf southwest of Penghu High, a thinner crust (25 to 30 km thick) is predicted at the location of the Zhu-I depocenter (Figure 7a). South of Zhu-I, crustal thickness values slightly increase to 30-35 km thick under the Dongsha High (Figure 7a). Note that the Penghu and Dongsha highs; although they do not form a continuous structure, are aligned along a NE-SW trend that marks the southeastern boundary of the present-day continental shelf.

South of the Penghu High, the crust progressively thins to less than 5 km thick. This hyper-thinned sector delineates a V-shape geometry of the SRS that terminates westward. The crustal architecture of this aborted rift system was previously captured on 2D reflection and refraction seismic profiles (e.g., Yeh et al., 2012; Lester et al., 2014; Liu et al., 2021; Mi et al., 2023) and regional gravity-derived crustal thickness maps (Gozzard et al., 2019); however, not at the high resolution herein presented (Figure 7a). Although floored by a thin crust, our gravity inversion does not predict an exhumed serpentinized mantle in the western SRS. On our map, areas of exhumed serpentinized mantle would potentially be predicted where the crust is ca. 3 km thick, equivalent to the mass deficiency of serpentinized mantle to the mantle (Cowie et al., 2015) (Figure 7a). Areas where the crust is 3 km or less are predicted near the Manilla trench; however, these predicted crustal thicknesses are expected to be too thin; close to the subduction zone, the reference Moho depth is expected to increase significantly, in which case the crust would be thicker.

A patch of thicker crust occurs between the SRS and the oceanic domain and corresponds to the SH. There, the crustal thickness generally exceeds 10 km thick and can locally reach more than 15 km thick. This thick crust coincides with the location of large seamounts mapped from seismic reflection data (Figure 3a and Figure 4c). Oceanward of the SH, the crust is thinner, decreasing to 6 km thickness. Away from the Manila Trench, little crustal thickness variation is seen, corresponding to the area where unequivocal oceanic crust has previously been identified (Gozzard et al., 2019).

Results assuming an age of 100 Ma for the lithosphere thermal re-equilibration are shown in Figure 7b. We only show the results in our area of interest, which includes SRS and

SH; a 33 Ma breakup age is regionally more consistent for the opening of the South China Sea (Briais et al., 1993; Larsen et al., 2018). An older age for the lithosphere thermal re-equilibration in the gravity inversion generates a deeper gravity-derived Moho and hence thicker predicted crust (Figure 7b).

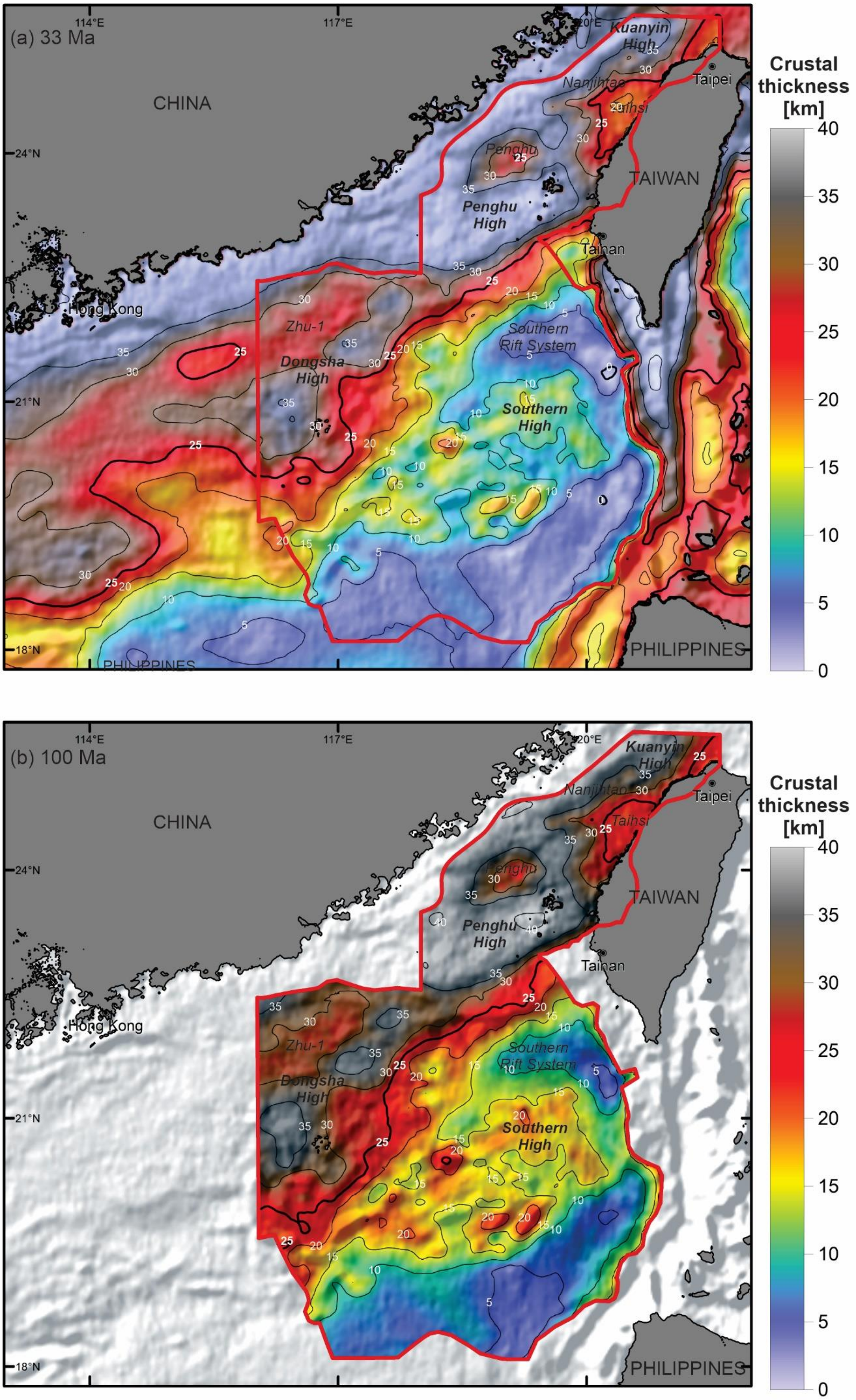
(a) 33 Ma
(b) 100 Ma
CHINA
TAIWAN
PHILIPPINES
Hong Kong
Taipei
Tainan
Kuanyin High
Nanjihtao
Taihsi
Penghu
Penghu High
Zhu-1
Dongsha High
Southern Rift System
Southern High
114°E
117°E
120°E
24°N
21°N
18°N
Crustal thickness [km]
40
35
30
25
20
15
10
5
0

Figure 7. Crustal thickness maps determined from gravity inversion. (a) Crustal thickness assuming an age of 33 Ma for the lithosphere thermal re-equilibration time (late Oligocene). Crustal thicknesses outside the area of exploration are calculated using the sediment thickness grid compiled in Gozzard et al. (2019). (b) Crustal thickness assuming a 100 Ma age for the lithosphere thermal re-equilibration time (late Lower Cretaceous). Contour lines mark 5 km intervals. Shaded relief free-air gravity is superimposed.

5.2 Joint Seismic-Gravity Inversion

We compare the Moho determined from gravity inversion for both end-member lithosphere thermal re-equilibration times (33 Ma and 100 Ma, Figure 7) with our seismic TWTT Moho interpretations along the 2D profiles (Figure 3). The gravity-inversion Moho, taken into the time domain, is shown in Figure 8.

For the younger age for lithosphere thermal re-equilibration (33 Ma), the Moho determined from gravity inversion is shallower than the seismic Moho TWTT (Figure 8a, c, e). This is more pronounced along the westernmost profile (Figure 8a) whereas both seismic and gravity-derived Moho TWTT become closer along the profiles located further to the east. Considering the older 100 Ma Mesozoic age of lithosphere thermal re-equilibration, gravity-derived Moho is deeper than our seismic Moho interpretation (Figure 8b, d, and f). Assuming that our top basement and seismic Moho interpretations correspond to the top and base of the crystalline basement, the difference between the gravity-derived Moho and seismic Moho TWTT indicates that the crust is either denser or lighter than the reference density considered in the gravity inversion scheme (2850 $kg.m^{-3}$). A gravity-derived Moho shallower than the seismic Moho indicates that the crust is on average denser than the reference density (2850 $kg.m^{-3}$), while a gravity-derived Moho deeper than the seismic Moho indicates that the crust is on average lighter than 2850 $kg.m^{-3}$.

The joint inversion method calculates the lateral variation of crustal densities and seismic velocities required to match the gravity-derived Moho with the interpreted seismic Moho in the time domain. We obtain 1) a profile showing lateral crustal density variations that are compared to the constant 2850 $kg.m^{-3}$ density initially used in the gravity inversion scheme (Figure 9), and 2) an adjusted trend for the Moho (Moho from joint inversion, Figure 8 and Figure 9). Both profiles show high-frequency variations that result from the influence of top basement topography in the method; longer wavelength trends are more meaningful.

Considering the younger 33 Ma age for lithosphere thermal re-equilibration, adjusted densities along the profiles are commonly above the average 2850 $kg.m^{-3}$ crust density. Average densities of ca. 2900 $kg.m^{-3}$ are observed over the SH (Figure 9), a result consistent with the thick (3 to 5 km thick) high velocity lower crust shown in refraction for the area (Eakin et al., 2014; Lester et al., 2014; Liu et al., 2021). A denser crust (ca. 2850 to 3000 $kg.m^{-3}$) is generally predicted for the SRS. Such a denser crust is not unexpected, as pointed out by the Vp/Vs analysis done nearby (Liu et al., 2023). We note, however, that densities predicted along our central line (Figure 9c and d) are lower compared to the two other profiles. This might result from uncertainty in our seismic Moho interpretation.

Considering the older 100 Ma age for lithosphere thermal re-equilibration, densities adjusted from our joint inversion method are commonly below the reference 2850 $kg.m^{-3}$ crust density (Figure 9b, d, f). Such low densities (~2700 $kg.m^{-3}$) could be explained if thick low-density sediments are present below the top basement pick and/or if the crust composition is dominantly felsic. Although seismic observations suggest that pre-rift sediments might locally be present below the top basement of the SRS (Figure 3), this is unlikely to be the case for the SH (Figure 4). Furthermore, considering that densities and seismic velocities are correlated, low crustal densities should correspond to slow seismic velocities. However, seismic refraction data ubiquitously show the presence of a thick (3 to 5 km thick) high-velocity lower crust layer (Eakin et al., 2014; Lester et al., 2014; S. Liu et al., 2018; Liu et al., 2021; Wang et al., 2006).

Although the exact age of the SRS cannot be constrained from our joint inversion method, a Cenozoic rifting age concerning the opening of the SCS is more consistent with seismic refraction velocity data.

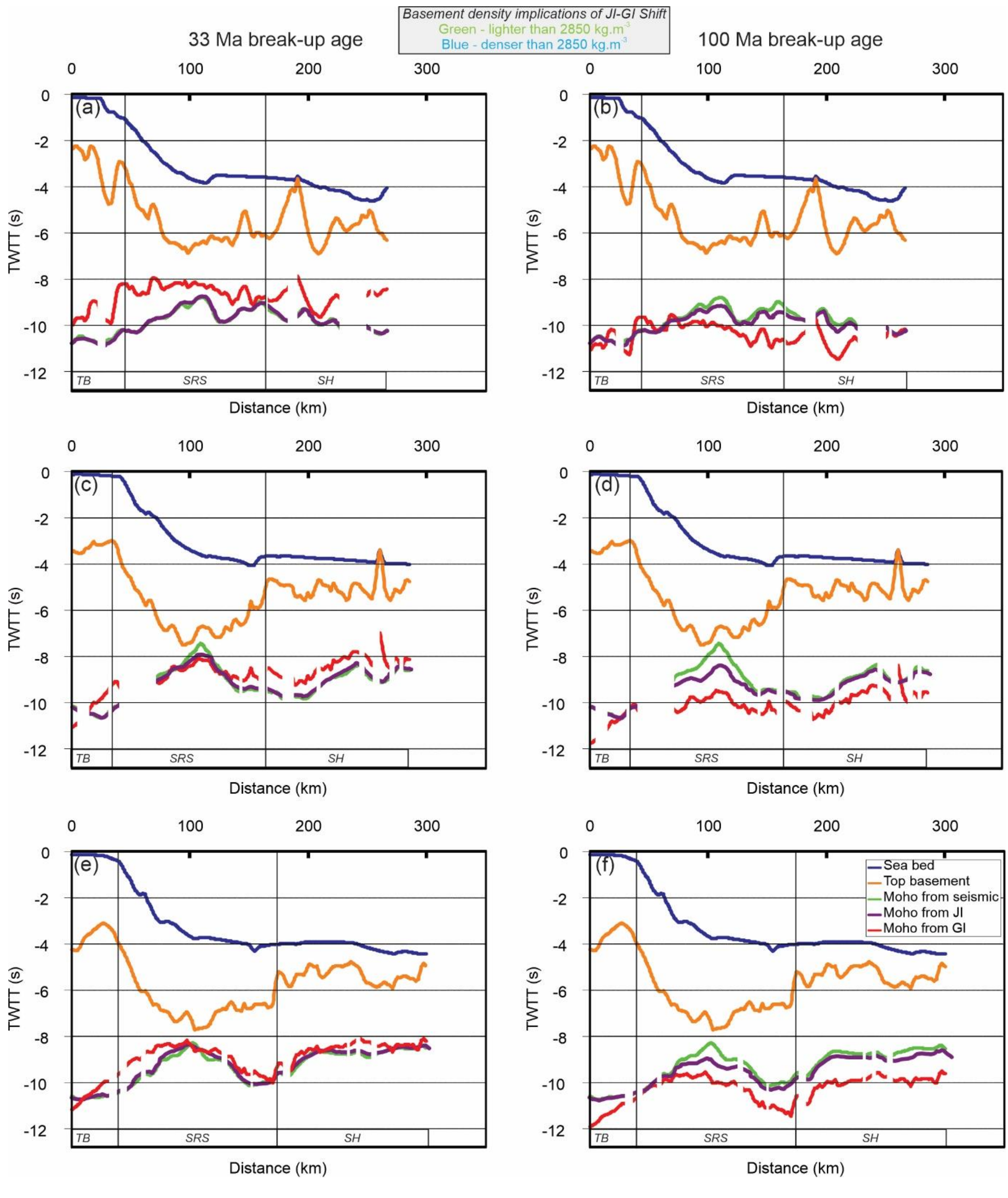

Figure 8. Selected profiles showing interpreted seafloor, top basement, and seismic Moho (where observed) in TWTT, and the Moho determined from gravity inversion taken into the time domain. The Moho resulting from the joint inversion of seismic and gravity data is also shown. Results for both 33 Ma (left column) and 100 Ma (right column) lithosphere thermal re-equilibration time are shown. (a) and (b) Composite section made with MGL0905-05 (N-S dip-oriented) and MGL0905-04 (W-E; strike-oriented). (c) and (d) Composite section made with MGL0905-22 (N-S dip-oriented), MGL0905-23(E-W; strike-oriented), and MGL0908-03 (N-S; dip-oriented). (e) and (f) Seismic line MGL0905-20 (N-S; dip-oriented). TB – Tainan Basin; SRS – Southern Rift System; SH – Southern High.

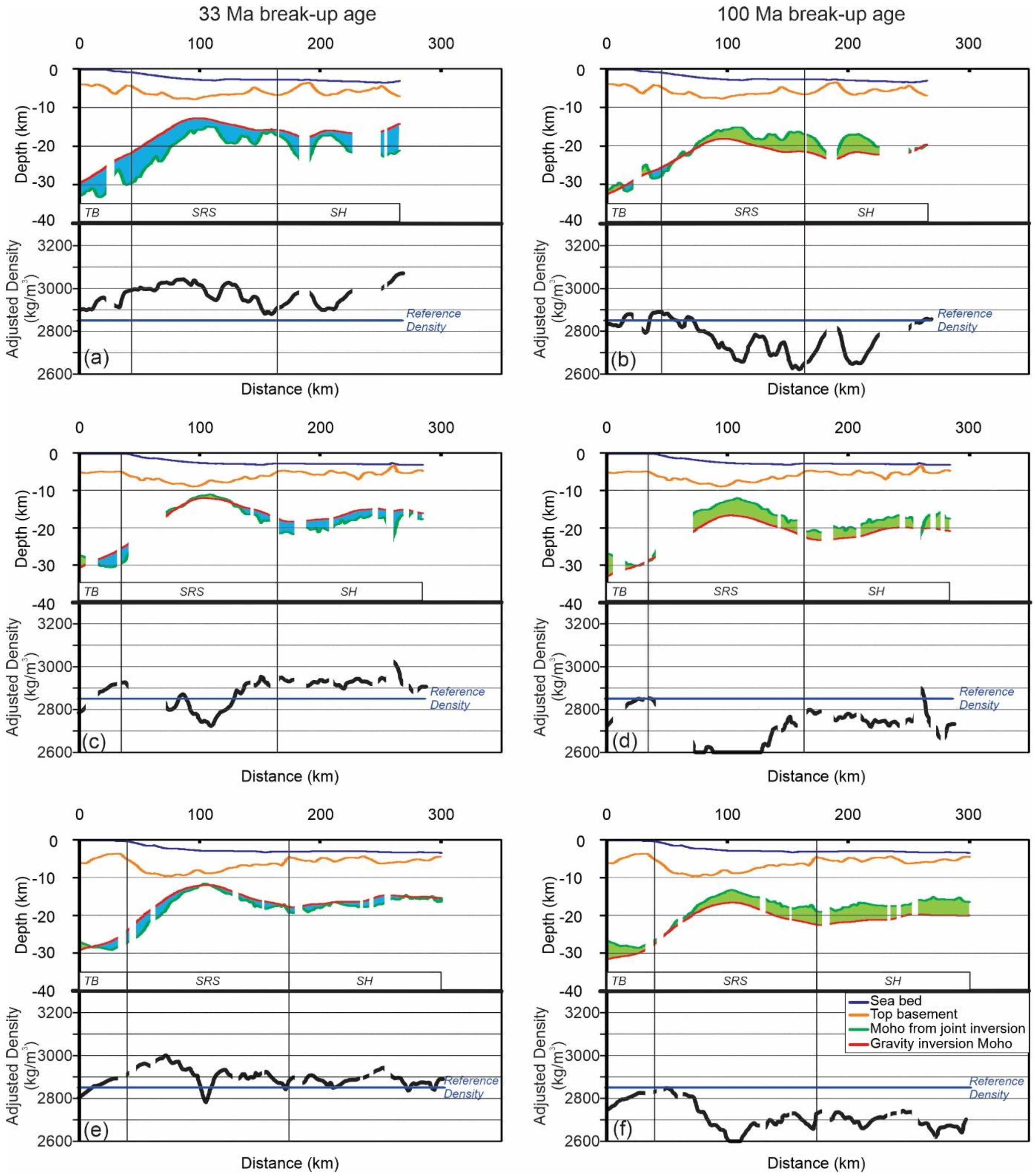

Figure 9. Results of the joint inversion of seismic and gravity Moho for selected profiles. For each profile, a depth section is shown as well as adjusted densities along profiles. The results are shown for both 33 Ma (left column) and 100 Ma (right column) lithosphere thermal re-equilibration time. (a) and (b) Composite section made with MGL0905-05 (N-S dip-oriented) and MGL0905-04 (W-E; strike-oriented). (c) and (d) Composite section made with MGL0905-22 (N-S dip-oriented), MGL0905-23(E-W; strike-oriented), and MGL0908-03 (N-S; dip-oriented). (e) and (f) Seismic line MGL0905-20 (N-S; dip-oriented). TB – Northern Rift System; SRS – Southern Rift System; SH – Southern High.

6. INTERPRETATIONS AND DISCUSSIONS

6.1. Crustal structure of the NE SCS distal margin: synthesis

The crustal structure and nature of the different domains of the NE SCS distal margin are still a matter of debate. Based on interpreted magnetic isochrons, the basement has already been categorized as an Eocene oceanic crust (Hsu et al., 2004) (Figure 10a). In contrast, the basement nature of the SRS has been interpreted as a thin continental crust under which mantle serpentinization might occur (Figure 10b) and overlaid by Mesozoic sediments (Figure 10c) (Liu et al., 2023, 2021). For the SH, controversy also exists with several proposed interpretations: (i) Mesozoic oceanic plateau (Xu et al., 2022) (Figure 10d), (ii) relicts of a Mesozoic thick oceanic crust (Reed, 1995; Sibuet et al., 2016; Yeh et al., 2012, 2010), (iii) part of the Philippine Plate oceanic crust (Hsu et al., 2004), and (iv) thin continental crust interspersed with magmatic additions (Figure 10f) (Bautista et al., 2001; Fan et al., 2017; Lester et al., 2014; Liu et al., 2023, 2021; Sibuet et al., 2016). Results of seismic observations combined with our new geophysical results enable us to discuss further the nature and evolution of these distinct distal structural domains. However, it is worth noting that the scenarios that fit our new geophysical analyses are not unique and need to be integrated with additional datasets including dredges and seismic interpretations.

Several hypotheses for the nature crust of the SRS have been tested that depend on the age of the lithosphere thermal re-equilibration (i.e. break-up ages) used in the gravity inversion (Figure 9). For a breakup age of 100 Ma, which corresponds to the opening of the Proto South China Sea (Dycoco et al., 2021 and references therein), the joint inversion gives crustal densities significantly lower than average crustal densities (Figure 9b). Opposite results are obtained when a breakup age of 33 Ma is assumed (opening of the South China Sea: Li et al., 2014 and references therein) (Figure 9a). Previous works recognized the SRS as a failed rift with or without oceanic spreading during the Eocene (e.g., Hsu et al., 2004; Lester et al., 2014) (Figure 10a, b, and c). An older Eocene age for this basin would result in a slightly lighter and thicker crust from the joint inversion compared to the 33 Ma break-up model (Figure 9a). The densities predicted for a Mesozoic age for the lithosphere thermal re-equilibration for the SRS suggest the occurrence of light rocks (i.e. sediments) in most of the crust. Such a scenario is not validated by refraction seismic data across this rift system, which shows velocities typical of upper crustal rocks (>5 km/s) (Eakin et al., 2014; Lester et al., 2014; Liu et al., 2021; McIntosh et al., 2005; Wan et al., 2017). So, it seems unlikely that the SRS was formed during the Mesozoic opening of the Proto South China Sea.

The 33 Ma break-up age corresponds to the rifting of the NE SCS and the opening of the Eastern subbasin of the South China Sea (Li et al., 2014). High-density values consistent with oceanic crust are obtained from the joint inversion method (Figure 9a). However, seismic reflection data shows the typical structure of a faulted rift system (Figure 3 - SRS). The SRS is most likely made of continental crust, with the likely occurrence of intermediate to mafic rocks, which is supported by previously interpreted data of Vp/Vs ratios (e.g., Liu et al., 2023), and refraction (e.g., Lester et al., 2014) (Figure 10b and c). Although no wells are available, Mesozoic pre-rift strata are likely present below the top basement mapped in the SRS (Figure 11). Stratiform reflectors and synform geometries truncated at the top basement (Tg) are observed on reflection seismic data (Figure 3). This sequence pinches out toward the BFZ and is no longer observable on seismic data further south (Figure 3b and c). This interpretation is consistent with drilling results and seismic data to the west in the so-called Chaoshan Basin, where Mesozoic high-velocities (3.5 and 5.5 km/s) sediments have been drilled (Fan et al., 2022). Velocities from refraction profiles (Eakin et al., 2014; Lester et al., 2014; S. Liu et al., 2018; Liu et al., 2021; McIntosh et al., 2005) that fit this range suggest the presence of high-velocity Mesozoic strata possible below Tg (Eakin et al., 2014; Lester et al., 2014; S. Liu et al., 2018; Liu et al., 2021; McIntosh et al., 2005). Gravity inversion results do not show any clear window of exhumed serpentinized mantle in the western part of SRS (Figure 7). Despite uncertainties on crustal thickness values near the subduction trench, our crustal thickness map shows a V-shape of the SRS, widening to the east and associated with a progressive crustal thinning, suggesting that SRS might correspond to a rift propagator (Figure 7). Based on these observations, we interpret that the SRS is made of continental rocks overlaid by Mesozoic sediments (Figure 10c and Figure 11).

We also tested the nature and age of the SH using the joint inversion method (Figure 9 and Figure 10d, e, and f). This domain is predicted to be denser than average crustal densities (i.e., dominantly mafic; Figure 7a and Figure 10d) only if it forms during or after the Cenozoic (33 Ma lithosphere thermal re-equilibration age, Figure 9a, c, e). Furthermore, refraction velocities of the SH show a good fit with a thick oceanic crust velocity profile (Figure 6a) (Mutter and Mutter, 1993). These results are consistent with our seismic observations of buried/outcropping seamounts, magmatic intrusions, and a possible occurrence of hydrothermal vent complexes (Figure 5). Miocene basalts were dredged at the Puyuan-Formosa seamount (Wang et al., 2012a, 2012b) (Figure 3a), suggesting that this magmatism might occur during the post-rift time. However, other dredged basalts from the Puyuan-Formosa and Beipo seamounts are of Mesozoic age (154.1 ±1.8 Ma and 93.2 ±5 Ma; whole-rock Ar-Ar) demonstrating that the basement was not fully formed at Cenozoic time (Xu et al., 2022) (Figure 3a). Considering a Mesozoic age of formation (i.e. joint inversion results for a lithosphere thermal re-equilibration of 100 Ma), predicted densities for the SH are lighter than the average crustal densities in which case, it would be made of rocks of felsic affinity or include thick sedimentary sequences (Figure 10e). Velocity-depth profiles from the SH are not very different from velocity envelopes compiled for the thin continental crust (Eakin et al., 2014; Lester et al., 2014; McIntosh et al., 2014) except for the additional presence of a high-velocity lower crust (Figure 6b). This lower crust shows a Vp/Vs ratio consistent with a mafic composition (possibly gabbroic) (Liu et al., 2023). It is therefore unlikely that the crust is dominantly felsic (Figure 10e). The crust of the SH is neither dominantly mafic (thick magmatic crust) (Figure 10d) nor felsic (continental crust) (Figure 10e) and a Mesozoic age of rifting can be excluded. Some scenarios can be disregarded for the nature and formation age of the SH: i) a Mesozoic oceanic plateau or Mesozoic thick oceanic crust (Figure 11d) (Hsu et al., 2004; Sibuet et al., 2004, 2002; Xu et al., 2022; Yeh et al., 2010) ii) Eocene to Oligocene oceanic crust (Figure 11a) (Hsu et al., 2004), and iii) thin continental crust (Figure 11e). Based on our results and similar to other propositions (Bautista et al., 2001; Eakin et al., 2014; Fan et al., 2017; Lester et al., 2014, 2013; C.-S. Liu et al., 2018; Liu et al., 2023; Wang et al., 2006; Yeh et al., 2012), we propose that the SH crust corresponds to a crust of polygenic origin (dredges of Mesozoic basalts) thinned during Cenozoic rifting and subsequently intruded by post-rift magmatism (Figure 10f) (Figure 11). As already inferred by Lester et al. (2014), these magmatic additions potentially masked rift-related normal faulting and pre-rift strata. It is worth noting that a magmatic crustal domain adjacent to the interpreted ocean-continent transition of the offshore conjugate Palawan margin shows similar high densities. However, it is interpreted as a thick oceanic crust (Franke et al., 2014).

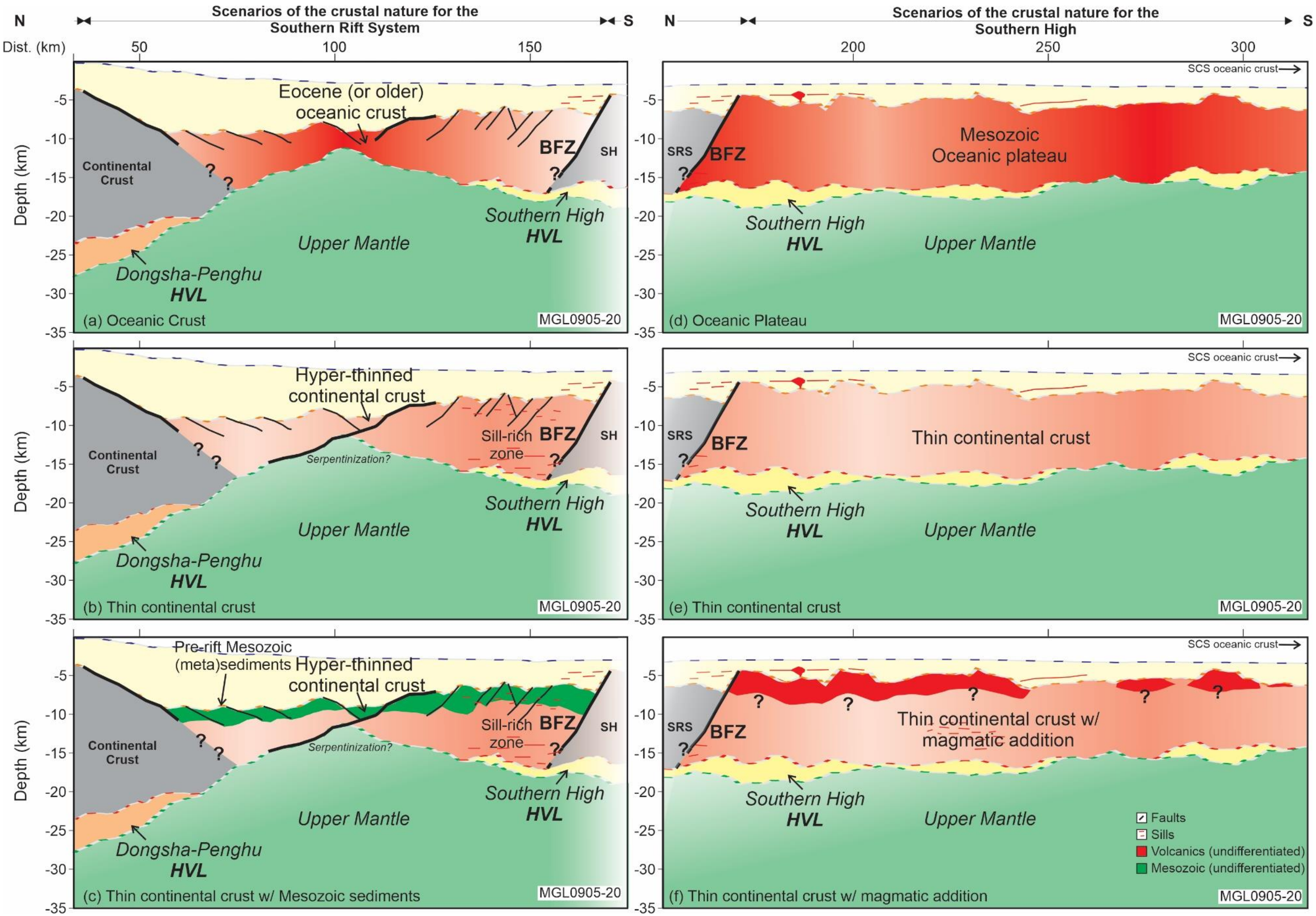

N
Scenarios of the crustal nature for the Southern Rift System
S
N
Scenarios of the crustal nature for the Southern High
S
Dist. (km)
50
100
150
200
250
300
Depth (km)
-5
-10
-15
-20
-25
-30
-35
SCS oceanic crust
Eocene (or older) oceanic crust
Continental Crust
BFZ
SH
Southern High HVL
Upper Mantle
Dongsha-Penghu HVL
(a) Oceanic Crust
MGL0905-20
SRS
Mesozoic Oceanic plateau
(d) Oceanic Plateau
Hyper-thinned continental crust
Sill-rich zone
Serpentinization?
(b) Thin continental crust
Thin continental crust
(e) Thin continental crust
Pre-rift Mesozoic (meta)sediments
(c) Thin continental crust w/ Mesozoic sediments
Thin continental crust w/ magmatic addition
(f) Thin continental crust w/ magmatic addition
Faults
Sills
Volcanics (undifferentiated)
Mesozoic (undifferentiated)

715

Figure 10. Geological scenarios for the crustal nature of the Southern Rift System (a, b, and c) and the Southern High (d, e, and f) based on seismic observations, gravity-inversion, and seismic-gravity joint inversion throughout the MGL0905-20 profile. **Southern Rift System (SRS)**: (a) Oceanic crust of Eocene (or older) age. (b) Hyper-thinned continental crust composed of crystalline rocks and, toward the south, punctual intrusion. (c) Hyper-thinned continental crust overlaid by Mesozoic Pre-rift (meta)-sediments. **Southern High (SH)**: (a) Mesozoic Mafic Crust. (b) Thin-continental crust. (c) Hybrid crust, that is, a thin continental crust with polyphasic magmatic addition.

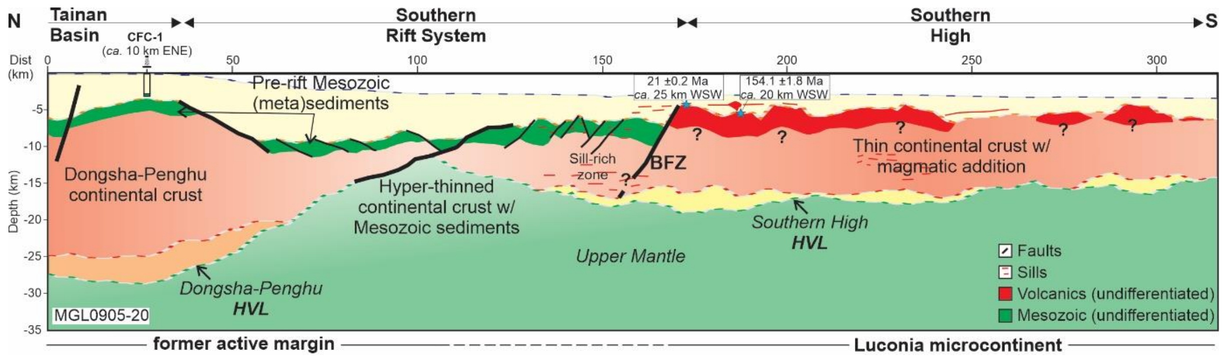

Figure 11. The crustal nature of the Northeastern South China Sea Margin. This figure is the merging of scenarios (c) and (f) from Figure 10 and is based on the geological/geophysical integration demonstrated in this study.

6.2. The origins of the NE SCS margin

The proximal NE SCS margin (i.e., the NRS) differs in terms of basement nature from the Tainan Basin and the distal NE SCS margin (i.e., the SRS and SH). Here we integrate our results in the frame of the Mesozoic active continental margin and discuss the implications for paleogeographic reconstruction.

The sampled crystalline basement of the NRS records an assemblage of Paleo-Mesozoic metamorphic and igneous rocks. The oldest record is from inherited zircons from andesites (437 ±13 Ma; U-Pb in zircon) (Chen et al., 2010) located at Penghu archipelago (Figure 12a). At the same location, rhyolite dykes and tuff-like rocks recorded Early Paleocene crystallization ages (58.7 ±0.8 Ma, and 63.3 ±1.5, U-Pb in zircon) (Chen et al., 2010). To the west, in the Zhu-1 area, several drilled wells also recovered granitoids samples that range from 153 Ma (Late Jurassic) to 70.5 Ma (Late Cretaceous) (Li et al., 2018; Shi et al., 2011; Xu et al., 2016) (Figure 12a). This igneous suite has a magmatic arc-related geochemical signature that suggests a Mesozoic continent-ocean subduction system (Yan et al., 2014) (Figure 12a). Similarly, refraction seismic profiles show the presence of an HVLC in the Dongsha and Penghu area interpreted as related to the former magmatic arc (Wan et al., 2017). These petrological and geophysical pieces of evidence suggest the development of a Mesozoic Andean-style magmatic arc (Savva et al., 2014) that represents nowadays the basement of the proximal NE SCS margin (i.e., NRS) (Figure 12b) (Fan et al., 2022; Li et al., 2018). Evidence for arc magmatism disappears further south towards the Tainan Basin (sensu strictu) (Figure 12a). There, several wells reached Mesozoic sedimentary strata (Figure 11 and Figure 12a) (Lu et al., 2014 and references therein). Similarly, in the adjacent Chaoshan Basin located further west, the well LF35-1-1 recorded Jurassic to Cretaceous sedimentary rocks (Shao et al., 2007) interpreted as deposited in a Mesozoic forearc setting (Figure 12a, b) (Fan et al., 2022). The interpreted Mesozoic strata of the SRS show folded geometries that might indicate it was formerly part of an accretionary wedge as proposed by Sibuet et al. (2002, 2004), similar to the nearby Chaoshan Basin (Figure 12b). At the interpreted boundary between the Mesozoic magmatic arc crustal domain and the forearc setting, the so-called positive South China Sea Magnetic Anomaly is observed and interpreted as a magnetic signature of the fossil arc (Li et al., 2018).

The SH is herein considered as a polygenic crust that underwent several magmatic pulses including volcanism as old as the Jurassic (Xu et al., 2022) (Figure 11). Basement complexes with similar geology (i.e., the occurrence of Mesozoic mafic rocks overlaying a Mesozoic or older continental crust) are observed in the Palawan Continental Block (Canto et al., 2012; Hashimoto, 1981; Knittel, 2011; Knittel et al., 2010; Knittel and Daniels, 1987). These two continental blocks (i.e., Palawan and Southern High) are conjugates and were part of the same terrane before the opening of the South China Sea. This interpretation is supported by geochemistry (Xu et al., 2022), plate kinematic (Advokaat and van Hinsbergen, 2024; Cao et al., 2022; Merdith et al., 2021; Müller et al., 2019; Scotese, 2016; Tian et al., 2021; Torsvik et al., 2019; Young et al., 2019), and paleotectonic (Hinz et al., 1991; Holloway, 1981, 1982; Sibuet et al., 2016; Taylor and Hayes, 1983) reconstructions. As the Palawan Continental Block has been assigned as part of the Luconia Microcontinent (Hall, 2012; Hall and Breitfeld, 2017; Pubellier and Sautter, 2022; Sautter and Pubellier, 2022), it is geologically reasonable to state that so does the SH (Figure 11) (Figure 12b). This implies that the crust of the SH is exotic compared to that of the Eurasian continent (Figure 12b). The Luconia Microcontinent represents the assemblage of several Mesozoic and older continental blocks that form not only the basement of Palawan and the SH but also of the Dangerous Ground (Hall, 2012; Madon, 1999). This microcontinent is believed to be docked in Laurasia between 90-80 Ma when subduction is terminated (Hall, 2012), and could explain the existence of Late Cretaceous basalts from the Beipo Seamount interpreted as emplaced during slab rollback (93.2 ±5 Ma, whole-rock Ar-Ar; Xu et al., 2022). Integrating the SH as part of the Luconia microcontinent hence implies that a suture zone is located somewhere between the Mesozoic magmatic arc and the SH (i.e., on Tainan and SRS) (Figure 12b) (Pubellier and Sautter, 2022; Sautter and Pubellier, 2022).

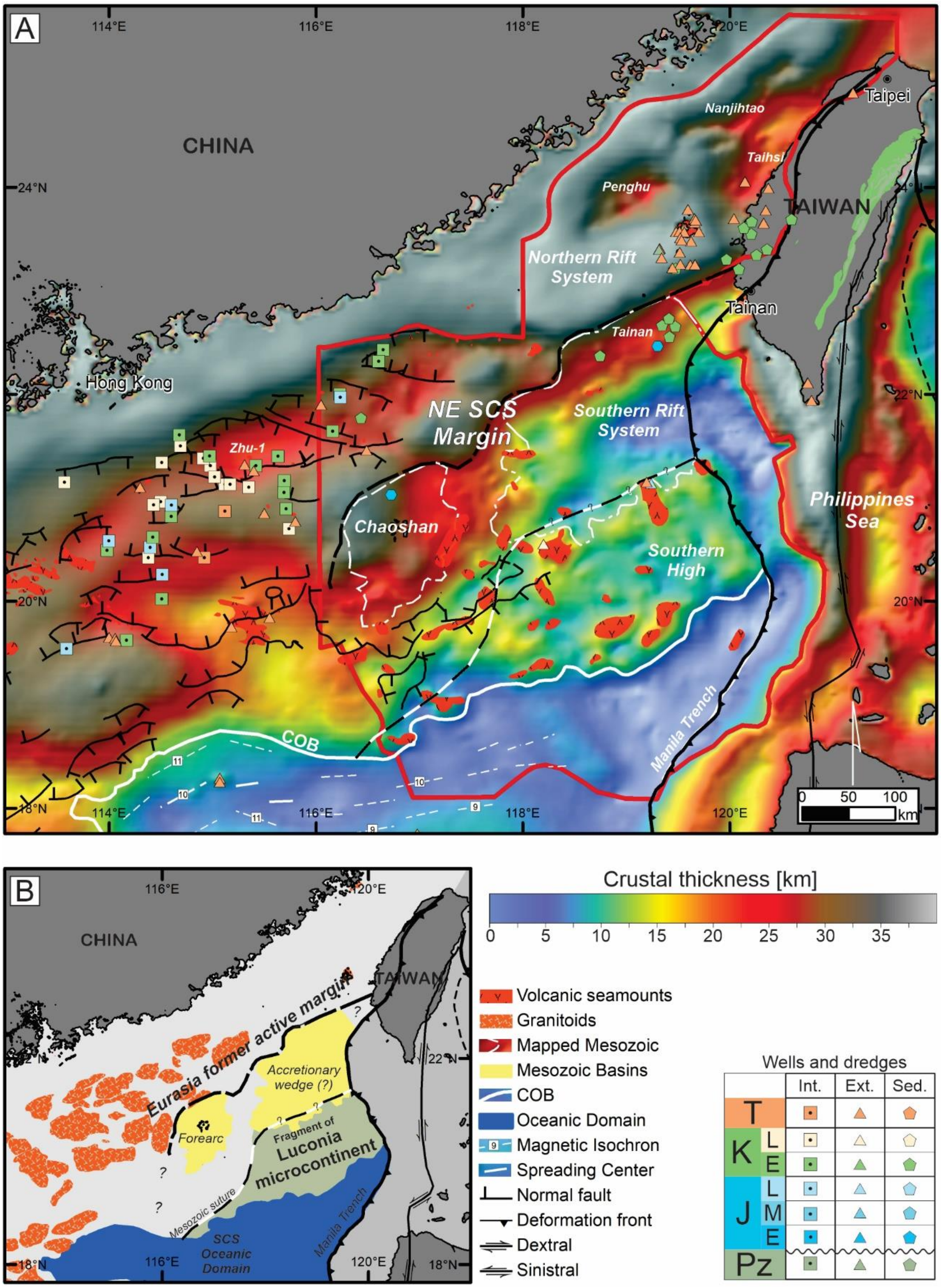

Figure 12. A - The tectonic-structural map of the NE South China Sea showing with the crustal thickness map (Model from the gravity-inversion using 33 Ma as break-up age) as background. COB – Continent-ocean boundary. B – Simplified map showing the main basement domains forming the framework of the NE SCS. Chaoshan Basin interpretation is according to Fan et al. (2022). Granitoids are according to Pubellier et al. (2016). Mesozoic suture is modified from Pubellier and Sautter (2022). Wells and dredges with information on the basement in Figure A are discretized according to the nature of the data: (i) squares from intrusives, (ii) triangles from extrusives, and (iii) hexagons from the

detrital analysis. These points are colored according to the ages obtained by radiometric analysis. For more information check the table in the bottom right of this figure.

7. CONCLUSIONS

In this paper, we investigate the crustal structure of the NE SCS rifted margin, which led to a reassessment of its nature and origins with implications for the Mesozoic and Cenozoic evolution of the South China Sea. To this end, we carried out a set of analyses including 3D gravity inversion and joint inversion of seismic and gravity data. We produced a set of interpreted seismic sections combined with crustal basement thickness maps and profiles showing lateral variations of crustal basement densities. The distal domain of the NE SCS rifted margin comprises two distinct domains.

The *Southern Rift System* (SRS) is characterized by thick Cenozoic sedimentary succession (3 to 7 km), including syn- and post-rift sediments, which overlies a hyper-thinned crust (<5 km). Mesozoic pre-rift strata showing folded geometries are possibly present below Tg as drilled in adjacent areas such as Tainan (*sensu strictu*) and Chaoshan basins. South of the rift axis, sparse volcanoes on the uppermost upper crust and sills are observed.

The *Southern High* (SH) is characterized by a thicker crust (3 to 5 s TWT; 10 to 15 km), and thin Cenozoic sedimentary succession (2-3 km). A 3 to 5 km thick HVLC is present, and the joint inversion of seismic and gravity Moho suggests that the crust is on average denser than 2850 $kg.m^{-3}$ considering a 33 Ma breakup age for the SCS. The combined analysis of geophysical and geological results, enables us to suggest that the SH consists of polygenic crust that underwent multi-episodic magmatism since the Mesozoic, including significant Cenozoic post-rift magmatism.

The NE SCS margin developed over a continental basement that was inherited from the previous Mesozoic active continental margin. Although the crust of the proximal margin shows evidence of an Eurasian affinity (Mesozoic magmatic arc), the pre-rift paleogeographic affinity of the distal margin is more debated. The similarity between the NE SCS and Palawan basement suggests that they might both be part of the Luconia microcontinent that collided with Eurasia during the Late Cretaceous. Our results suggest that the Cenozoic rift developed over a Mesozoic collisional system at the location of a former suture zone between Eurasia and Luconia.

ACKNOWLEDGMENTS

The authors are grateful to the Marine Geoscience Data System, the TOPEX online repository, the International Ocean Discovery Program (IODP), and the Deep Sea Drilling Project (DSDP) for providing the open-source data used in this study. Mateus Rodrigues de Vargas thanks CY Cergy-Paris Université for providing him with the Ph.D. grant. We acknowledge Neuralog and Schlumberger for providing Academic Licenses for their commercial software. The manuscript benefited from the constructive remarks of all ANR/Collisea's team (grant number ANR-22-CE49-0015) and their insightful discussions about the South China Sea evolution.

DATA AVAILABILITY STATEMENT

The authors comply with the AGU's data policy. The data sets used in this paper are open. Seismic reflection lines from the Marine Geoscience Data System are available at https://www.marine-geo.org/. Free air gravity anomaly and topography data were obtained from the TOPEX online repository of the Scripps Institution of Oceanography, University of California, San Diego. Topex Gravity Anomaly (V29.1 for gravity and V19.1 for topography) is available at https://topex.ucsd.edu/cgi-bin/get_data.cgi, while Topex topographic data (V2.3) at https://topex.ucsd.edu/cgi-bin/get_srtm15.cgi. Data sets from the International Ocean Discovery Program (IODP), and the Deep Sea Drilling Project (DSDP) are available at, respectively, https://web.iodp.tamu.edu/LORE/, and https://brg.ldeo.columbia.edu/logdb/.

REFERENCES

Advokaat, E.L., van Hinsbergen, D.J.J., 2024. Finding Argoland: Reconstructing a microcontinental archipelago from the SE Asian accretionary orogen. *Gondwana Research*, 128, 161–263. https://doi.org/10.1016/j.gr.2023.10.005

Alvey, A., Gaina, C., Kusznir, N.J., Torsvik, T.H., 2008. Integrated crustal thickness mapping and plate reconstructions for the high Arctic. *Earth and Planetary Science Letters*, 274, 310–321. https://doi.org/10.1016/J.EPSL.2008.07.036

Barckhausen, U., Engels, M., Franke, D., Ladage, S., Pubellier, M., 2014. Evolution of the South China Sea: Revised ages for breakup and seafloor spreading. *Marine and Petroleum Geology*, 58, 599–611. https://doi.org/10.1016/j.marpetgeo.2014.02.022

Barckhausen, U., Roeser, H.A., 2004. Seafloor Spreading Anomalies in the South China Sea Revisited. *Geophysical Monograph Series*, 149, 121–125. https://doi.org/10.1029/149GM07

Bautista, B.C., Bautista, M.L.P., Oike, K., Wu, F.T., Punongbayan, R.S., 2001. A new insight on the geometry of subducting slabs in northern Luzon, Philippines. *Tectonophysics*, 339, 279–310. https://doi.org/10.1016/S0040-1951(01)00120-2

Birch, F., 1964. Density and composition of mantle and core. *Journal of Geophysical Research*, 69, 4377–4388. https://doi.org/10.1029/jz069i020p04377

Bird, P., 2003. An updated digital model of plate boundaries. *Geochemistry, Geophysics, Geosystems*, 4. https://doi.org/10.1029/2001GC000252

Briais, A., Patriat, P., Tapponnier, P., 1993. Updated interpretation of magnetic anomalies and seafloor spreading stages in the South China Sea: Implications for the Tertiary tectonics of Southeast Asia. *Journal of Geophysical Research: Solid Earth*, 98, 6299–6328. https://doi.org/10.1029/92JB02280

Canto, A.P.B., Padrones, J.T., Concepcion, R.A.B., Perez, A.D.C., Tamayo, R.A., Dimalanta, C.B., Faustino-Eslava, D. V., Queaño, K.L., Yumul, G.P., 2012. Geology of northwestern Mindoro and its offshore islands: Implications for terrane accretion in west Central Philippines. *Journal of Asian Earth Sciences*, 61, 78–87. https://doi.org/10.1016/j.jseaes.2012.08.006

Cao, X., Zahirovic, S., Li, S., Suo, Y., Wang, P., Liu, J., Müller, R.D., 2022. A deforming plate tectonic model of the South China Block since the Jurassic. *Gondwana Research*, 102, 3–16. https://doi.org/10.1016/j.gr.2020.11.010

Chappell, A.R., Kusznir, N.J., 2008. Three-dimensional gravity inversion for Moho depth at rifted continental margins incorporating a lithosphere thermal gravity anomaly correction. *Geophysical Journal International*, 174, 1–13. https://doi.org/10.1111/J.1365-246X.2008.03803.X/2/174-1-1-FIG010.JPEG

Chen, C.H., Hsieh, P.S., Wang, K.L., Yang, H.J., Lin, W., Liang, Y.H., Lee, C.Y., Yang, H.C., 2010. Zircon LA-ICPMS U-Pb ages and Hf isotopes of Huayu (Penghu Islands) volcanics in the Taiwan Strait and tectonic implication. *Journal of Asian Earth Sciences*, 37, 17–30. https://doi.org/10.1016/j.jseaes.2009.07.003

Chen, C.H., Lee, C.-Y., Huang, T.-C., Ting, J.-S., 1997. Radiometric Ages and Petrological and Geochemical Aspects of Some Late Cretaceous and Paleogene Volcanic Rocks beneath the Northern Offshore Taiwan. *Petroleum Geology of Taiwan*, 31, 61–88.

Chung, S.L., Sun, S. su, Tu, K., Chen, C.H., Lee, C. yu, 1994. Late Cenozoic basaltic volcanism around the Taiwan Strait, SE China: Product of lithosphere-asthenosphere interaction during continental extension. *Chemical Geology*, 112, 1–20. https://doi.org/10.1016/0009-2541(94)90101-5

Cowie, L., Angelo, R.M., Kusznir, N., Manatschal, G., Horn, B., 2017. Structure of the ocean-continent transition, location of the continent-ocean boundary and magmatic type of the northern Angolan margin from integrated quantitative analysis of deep seismic reflection and gravity anomaly data. *Geological Society Special Publication*, 438, 159–176. https://doi.org/10.1144/SP438.6

Cowie, L., Kusznir, N., Manatschal, G., 2015. Determining the COB location along the Iberian margin and Galicia Bank from gravity anomaly inversion, residual depth anomaly and subsidence analysis. *Geophysical Journal International*, 203, 1355–1372. https://doi.org/10.1093/gji/ggv367

Divins, D.L., 2003. Total Sediment Thickness of the World’s Oceans and Marginal Seas.

Dycoco, J.M.A., Payot, B.D., Valera, G.T. V., Labis, F.A.C., Pasco, J.A., Perez, A.D.C., Tani, K., 2021. Juxtaposition of Cenozoic and Mesozoic ophiolites in Palawan island, Philippines: New insights on the evolution of the Proto-South China Sea. *Tectonophysics*, 819, 229085. https://doi.org/10.1016/j.tecto.2021.229085

Eakin, D.H., McIntosh, K.D., Van Avendonk, H.J.A., Lavier, L., Lester, R., Liu, C.S., Lee, C.S., 2014. Crustal-scale seismic profiles across the Manila subduction zone: The transition from intraoceanic subduction to incipient collision. *Journal of Geophysical Research: Solid Earth*, 119, 1–17. https://doi.org/10.1002/2013JB010395

Fan, C., Xia, S., Cao, J., Zhao, F., Wan, K., 2022. Seismic constraints on a remnant Mesozoic forearc basin in the northeastern South China Sea. *Gondwana Research*, 102, 77–94. https://doi.org/10.1016/j.gr.2020.10.006

Fan, C., Xia, S., Zhao, F., Sun, J., Cao, J., Xu, H., Wan, K., 2017. New insights into the magmatism in the northern margin of the South China Sea: Spatial features and volume of intraplate seamounts. *Geochemistry, Geophysics, Geosystems*, 18, 2216–2239. https://doi.org/10.1002/2016GC006792

Franke, D., Savva, D., Pubellier, M., Steuer, S., Mouly, B., Auxietre, J.L., Meresse, F., Chamot-Rooke, N., 2014. The final rifting evolution in the South China Sea. *Marine and Petroleum Geology*, 58, 704–720. https://doi.org/10.1016/j.marpetgeo.2013.11.020

Gong, Z., Li, S., Xie, T., Zhang, Q.M., Xu, S.C., Xia, K.Y. (Eds.), 1997. Continental margin basin analysis and hydrocarbon accumulation of the northern South China Sea, Science Press. Science Press, Beijing, China.

Gozzard, S., Kusznir, N., Franke, D., Cullen, A., Reemst, P., Henstra, G., 2019. South China Sea crustal thickness and oceanic lithosphere distribution from satellite gravity inversion. *Petroleum Geoscience*, 25, 112–128. https://doi.org/10.1144/petgeo2016-162

Greenhalgh, E.E., Kusznir, N.J., 2007. Evidence for thin oceanic crust on the extinct Aegir Ridge, Norwegian Basin, NE Atlantic derived from satellite gravity inversion. *Geophysical Research Letters*, 34. https://doi.org/10.1029/2007GL029440

Hall, R., 2012. Late Jurassic-Cenozoic reconstructions of the Indonesian region and the Indian Ocean. *Tectonophysics*, 570–571, 1–41. https://doi.org/10.1016/j.tecto.2012.04.021

Hall, R., Breitfeld, H.T., 2017. Nature and demise of the Proto-South China Sea. *Bulletin of the Geological Society of Malaysia*, 63, 61–76. https://doi.org/10.7186/bgsm63201703

Harkin, C., Kusznir, N., Tugend, J., Manatschal, G., McDermott, K., 2019. Evaluating magmatic additions at a magma-poor rifted margin: An East Indian case study. *Geophysical Journal International*, 217, 25–40. https://doi.org/10.1093/gji/ggz007

Hashimoto, W., 1981. Geologic development of the Philippines, in: Kobayashi, T., Toriyama, R., Hashimoto, W. (Eds.), Geology and Paleontology of Southeast Asia. University of Tokio Press, Tokyo, Japan, pp. 83–170.

Hayes, D., 2011a. Multi-Channel Seismic Shot Data from the Philippine Sea acquired during the R/V Robert D. Conrad expedition RC2006 (1976), Interdisciplinary Earth Data Alliance (IEDA).

Hayes, D., 2011b. Multi-Channel Seismic Shot Data from the Philippine Sea acquired during the R/V Vema expedition V3613 (1980), Interdisciplinary Earth Data Alliance (IEDA). https://doi.org/10.1594/IEDA/317105

Hayes, D.E., 2015. Raw Seismic Shot Time Navigation Data from the South China Sea acquired during the Robert D. Conrad expedition RC2612 (1985), Interdisciplinary Earth Data Alliance (IEDA). https://doi.org/10.1594/IEDA/321924

Hinz, K., Block, M., Kudrass, H.R., Meyer, H., 1991. Structural Elements of the Sulu Sea, Philippines. *Geologisches Jahrbuch*, Reihe A, 483–506.

Holloway, N.H., 1982. North Palawan Block, Philippines—Its Relation to Asian Mainland and Role in Evolution of South China Sea. *AAPG Bulletin*, 66, 1355–1383. https://doi.org/10.1306/ad461449-16f7-11d7-8645000102c1865d

Holloway, N.H., 1981. The North Palawan Block, Philippines: its relation to the Asian Mainland and its role in the evolution of the South China Sea. *Geological Society of Malaysia*, 14, 19–58. https://doi.org/10.1306/03B5A7A5-16D1-11D7-8645000102C1865D

Hsu, S.K., Yeh, Y.C., Doo, W. Bin, Tsai, C.H., 2004. New bathymetry and magnetic lineations identifications in the northernmost South China Sea and their tectonic implications. *Marine Geophysical Research*, 25, 29–44. https://doi.org/10.1007/s11001-005-0731-7

Hu, B., Wang, L., Yan, W., Liu, S., Cai, D., Zhang, G., Zhong, K., Pei, J., Sun, B., 2013. The tectonic evolution of the Qiongdongnan Basin in the northern margin of the South China Sea. *Journal of Asian Earth Sciences*, 77, 163–182. https://doi.org/10.1016/J.JSEAES.2013.08.022

Huang, C.Y., Yen, Y., Zhao, Q.H., Lin, C.T., 2012. Cenozoic stratigraphy of Taiwan: Window into rifting, stratigraphy and paleoceanography of South China Sea. *Chinese Science Bulletin*, 57, 3130–3149. https://doi.org/10.1007/s11434-012-5349-y

Jamtveit, B., Svensen, H., Podladchikov, Y.Y., Planke, S., 2004. Hydrothermal vent complexes associated with sill intrusions in sedimentary basins. *Geological Society, London, Special Publications*, 234, 233–241. https://doi.org/10.1144/GSL.SP.2004.234.01.15

Juang, W.S., Chen, J.C., 1992. Geochronology and geochemistry of Penghu basalts, Taiwan Strait and their tectonic significance. *Journal of Southeast Asian Earth Sciences*, 7, 185–193. https://doi.org/10.1016/0743-9547(92)90053-E

Karner, G.D., Johnson, C., Shoffner, J., Lawson, M., Sullivan, M., Sitgreaves, J., McHarge, J., Stewart, J., Figueredo, P., 2022. Chapter 9: Tectono-Magmatic Development of the Santos and Campos Basins, Offshore Brazil. *Memoir 124: The Supergiant Lower Cretaceous Pre-Salt Petroleum Systems of the Santos Basin, Brazil*, 215–256. https://doi.org/10.1306/13722321msb.9.1853

Knittel, U., 2011. 83 Ma rhyolite from Mindoro - evidence for Late Yanshanian magmatism in the Palawan Continental Terrane (Philippines). *Island Arc*, 20, 138–146. https://doi.org/10.1111/j.1440-1738.2010.00744.x

Knittel, U., Daniels, U., 1987. Sr-isotopic composition of marbles from the Puerto Galera area (Mindoro, Philippines): Additional evidence for a Paleozoic age of a metamorphic complex in the Philippine island arc. *Geology*, 15, 136–138. https://doi.org/10.1130/0091-7613(1987)15<136:SCOMFT>2.0.CO;2

Knittel, U., Hung, C.H., Yang, T.F., Iizuka, Y., 2010. Permian arc magmatism in Mindoro, the Philippines: An early Indosinian event in the Palawan Continental Terrane. *Tectonophysics*, 493, 113–117. https://doi.org/10.1016/j.tecto.2010.07.007

Kusznir, N.J., Roberts, A.M., Alvey, A.D., 2018. Crustal structure of the conjugate Equatorial Atlantic Margins, derived by gravity anomaly inversion. *Geological Society, London, Special Publications*, 476, 83–107. https://doi.org/10.1144/SP476.5

Lee, T.-Y., Tang, C.-H., Ting, J.-S., Yeong-Yaw, H., 1993. Sequence Stratigraphy of the Tainan Basin, Offshore Southwestern Taiwan. *Petroleum Geology of Taiwan*, 28, 119–158.

Lei, C., Ren, J., Pang, X., Chao, P., Han, X., 2018. Continental rifting and sediment infill in the distal part of the northern South China Sea in the Western Pacific region: Challenge on the present-day models for the passive margins. *Marine and Petroleum Geology*, 93, 166–181. https://doi.org/10.1016/j.marpetgeo.2018.02.020

Lester, R., McIntosh, K., 2012. Multiple attenuation in crustal-scale imaging: Examples from the TAIGER marine reflection data set. *Marine Geophysical Research*, 33, 289–305. https://doi.org/10.1007/s11001-012-9149-1

Lester, R., McIntosh, K., Van Avendonk, H.J.A., Lavier, L., Liu, C.S., Wang, T.K., 2013. Crustal accretion in the Manila trench accretionary wedge at the transition from subduction to mountain-building in Taiwan. *Earth and Planetary Science Letters*, 375, 430–440. https://doi.org/10.1016/J.EPSL.2013.06.007

Lester, R., Van Avendonk, H.J.A., McIntosh, K., Lavier, L., Liu, C. -S., Wang, T.K., Wu, F., 2014. Rifting and magmatism in the northeastern South China Sea from wide-angle tomography and seismic reflection imaging. *Journal of Geophysical Research: Solid Earth*, 119, 2305–2323. https://doi.org/10.1002/2013JB010639

Leyden, R., 2015. Raw Multi-Channel Seismic Shot Time Navigation Data from the South China Sea acquired during the Vema expedition V3614 (1980). *Interdisciplinary Earth Data Alliance (IEDA)*, . https://doi.org/10.1594/IEDA/321915

Li, C.-F., Lin, J., Kulhanek, D.K., Williams, T., Bao, R., Briais, A., Brown, E.A., Chen, Y., Clift, P.D., Colwell, F.S., Dadd, K.A., Ding, W.-W., Hernández-Almeida, I., Huang, X.-L., Hyun, S., Jiang, T., Koppers, A.A.P., Li, Q., Liu, C., Liu, Q., Liu, Z., Nagai, R.H., Peleo-Alampay, A., Su, X., Sun, Z., Tejada, M.L.G., Trinh, H.S., Yeh, Y.-C., Zhang, C., Zhang, F., Zhang, G.-L., Zhao, X., 2015. Expedition 349 summary 349. https://doi.org/10.14379/iodp.proc.349.101.2015

Li, C.-F., Xu, X., Lin, J., Sun, Z., Zhu, J., Yao, Y., Zhao, X., Liu, Q., Kulhanek, D.K., Wang, J., Song, T., Zhao, J., Qiu, N., Guan, Y., Zhou, Z., Williams, T., Bao, R., Briais, A., Brown, E.A., Chen, Y., Clift, P.D., Colwell, F.S., Dadd, K.A., Ding, W., Almeida, I.H., Huang, X.-L., Hyun, S., Jiang, T., Koppers, A.A.P., Li, Q., Liu, C., Liu, Z., Nagai, R.H., Peleo-Alampay, A., Su, X., Tejada, M.L.G., Trinh, H.S., Yeh, Y.-C., Zhang, C., Zhang, F., Zhang, G.-L., 2014. Ages and magnetic structures of the South China Sea constrained by deep tow magnetic surveys and IODP Expedition 349. *Geochemistry, Geophysics, Geosystems*, 15, 4958–4983. https://doi.org/10.1002/2014GC005567

Li, F., Sun, Z., Yang, H., 2018. Possible Spatial Distribution of the Mesozoic Volcanic Arc in the Present-Day South China Sea Continental Margin and Its Tectonic Implications. *Journal of Geophysical Research: Solid Earth*, 123, 6215–6235. https://doi.org/10.1029/2017JB014861

Lin, A.T., Watts, A.B., Hesselbo, S.P., 2003. Cenozoic stratigraphy and subsidence history of the South China Sea margin in the Taiwan region. *Basin Research*, 15, 453–478. https://doi.org/10.1046/j.1365-2117.2003.00215.x

Lin, A.T., Yang, C.C., Wang, M.H., Wu, J.C., 2021. Oligocene-Miocene sequence stratigraphy in the northern margin of the South China Sea: An example from Taiwan. *Journal of Asian Earth Sciences*, 213, 104765. https://doi.org/10.1016/j.jseaes.2021.104765

Lin, C.-W., Chen, W.-S., 2016. Geological Map of Taiwan 1:400000. Geological Society of Taiwan, Taipei.

Liu, C.-S., Wu, F., McIntosh, K., Van Avendonk, H., 2018. Multi-Channel Seismic Shot Data from the Philippine Sea acquired during R/V Marcus G. Langseth expedition MGL0905 (2009), Interdisciplinary Earth Data Alliance (IEDA). https://doi.org/10.1594/IEDA/310283

Liu, S., Zhao, M., Sibuet, J.C., Qiu, X., Wu, J., Zhang, J., Chen, C., Xu, Y., Sun, L., 2018. Geophysical constraints on the lithospheric structure in the northeastern South China Sea and its implications for the South China Sea geodynamics. *Tectonophysics*, 742–743, 101–119. https://doi.org/10.1016/J.TECTO.2018.06.002

Liu, Y., Li, C.F., Qiu, X., Zhang, J., 2023. Vp/Vs ratios beneath a hyper-extended failed rift support a magma-poor continental margin in the northeastern South China Sea. *Tectonophysics*, 846, 229652. https://doi.org/10.1016/j.tecto.2022.229652

Liu, Y., Li, C.F., Wen, Y., Yao, Z., Wan, X., Qiu, X., Zhang, J.Z., Abbas, A., Peng, X., Li, G., 2021. Mantle serpentinization beneath a failed rift and post-spreading magmatism in the northeastern South China Sea margin. *Geophysical Journal International*, 225, 811–828. https://doi.org/10.1093/gji/ggab006

Lu, B., Wang, P., Wu, J., Li, W., Wang, W., Lang, Y., 2014. Distribution of the mesozoic in the continental margin basins of the South China sea and its petroliferous significance. *Petroleum Exploration and Development*, 41, 545–552. https://doi.org/10.1016/S1876-3804(14)60065-3

Madon, M., 1999. Geological Setting of Sarawak, in: The Petroleum Geology and Resources of Malaysia. Petroliam Nasional Berhad (PETRONAS), Kuala Lumpur, pp. 273–290.

Magee, C., Hunt-Stewart, E., Jackson, C.A.-L., 2013. Volcano growth mechanisms and the role of sub-volcanic intrusions: Insights from 2D seismic reflection data. *Earth and*

Planetary Science Letters, 373, 41–53. https://doi.org/10.1016/j.epsl.2013.04.041

Magee, C., Maharaj, S.M., Wrona, T., Jackson, C.A.L., 2015. Controls on the expression of igneous intrusions in seismic reflection data. *Geosphere*, 11, 1024–1041. https://doi.org/10.1130/GES01150.1

Magee, C., Stevenson, C.T.E., Ebmeier, S.K., Keir, D., Hammond, J.O.S., Gottsmann, J.H., Whaler, K.A., Schofield, N., Jackson, C.A.-L., Petronis, M.S., O'Driscoll, B., Morgan, J., Cruden, A., Vollgger, S.A., Dering, G., Micklethwaite, S., Jackson, M.D., 2018. Magma Plumbing Systems: A Geophysical Perspective. *Journal of Petrology*, 59, 1217–1251. https://doi.org/10.1093/petrology/egy064

McIntosh, K., Hsu, S.-K., Van Avendonk, H., 2017. Multi-Channel Seismic Shot Data from the Philippine Sea acquired during R/V Marcus G. Langseth expedition MGL0908 (2009), Interdisciplinary Earth Data Alliance (IEDA).

McIntosh, K., Lavier, L., Van Avendonk, H., Lester, R., Eakin, D., Liu, C.S., 2014. Crustal structure and inferred rifting processes in the northeast South China Sea. *Marine and Petroleum Geology*, 58, 612–626. https://doi.org/10.1016/j.marpetgeo.2014.03.012

McIntosh, K., Nakamura, Y., Wang, T.K., Shih, R.C., Chen, A., Liu, C.S., 2005. Crustal-scale seismic profiles across Taiwan and the western Philippine Sea. *Tectonophysics*, 401, 23–54. https://doi.org/10.1016/j.tecto.2005.02.015

Merdith, A.S., Williams, S.E., Collins, A.S., Tetley, M.G., Mulder, J.A., Blades, M.L., Young, A., Armistead, S.E., Cannon, J., Zahirovic, S., Müller, R.D., 2021. Extending full-plate tectonic models into deep time: Linking the Neoproterozoic and the Phanerozoic. *Earth-Science Reviews*, 214, 103477. https://doi.org/10.1016/j.earscirev.2020.103477

Mi, L., Deng, H., Gouiza, M., Yang, H., Sun, Q., Sun, S., Dong, F., 2023. Crust necking of the northeastern South China Sea: Insights from deep seismic data. *Italian Journal of Geosciences*, 142, 57–82. https://doi.org/10.3301/IJG.2023.06

Morley, C.K., 2016. Major unconformities/termination of extension events and associated surfaces in the South China Seas: Review and implications for tectonic development. *Journal of Asian Earth Sciences*, 120, 62–86. https://doi.org/10.1016/j.jseaes.2016.01.013

Müller, R.D., Zahirovic, S., Williams, S.E., Cannon, J., Seton, M., Bower, D.J., Tetley, M.G., Heine, C., Le Breton, E., Liu, S., Russell, S.H.J., Yang, T., Leonard, J., Gurnis, M.,

2019. A Global Plate Model Including Lithospheric Deformation Along Major Rifts and Orogens Since the Triassic. *Tectonics*, 38, 1884–1907. https://doi.org/10.1029/2018TC005462

Mutter, C.Z., Mutter, J.C., 1993. Variations in thickness of layer 3 dominate oceanic crustal structure. *Earth and Planetary Science Letters*, 117, 295–317. https://doi.org/10.1016/0012-821X(93)90134-U

Nirrengarten, M., Mohn, G., Kusznir, N.J., Sapin, F., Despinois, F., Pubellier, M., Chang, S.P., Larsen, H.C., Ringenbach, J.C., 2020. Extension modes and breakup processes of the southeast China-Northwest Palawan conjugate rifted margins. *Marine and Petroleum Geology*, 113, 104123. https://doi.org/10.1016/j.marpetgeo.2019.104123

Nissen, S.S., Hayes, D.E., Buhl, P., Diebold, J., Bochu, Y., Zeng, W., Chen, Y., 1995. Deep penetration seismic soundings across the northern margin of the South China Sea. *Journal of Geophysical Research: Solid Earth*, 100, 22407–22433. https://doi.org/10.1029/95JB01866

Parker, R.L., 1972. The Rapid Calculation of Potential Anomalies. *Geophysical Journal International*, 31, 447–455. https://doi.org/10.1111/j.1365-246X.1973.tb06513.x

Pin, Y., Di, Z., Zhaoshu, L., 2001. A crustal structure profile across the northern continental margin of the South China Sea. *Tectonophysics*, 338, 1–21. https://doi.org/10.1016/S0040-1951(01)00062-2

Planke, S., Millett, J.M., Maharjan, D., Jerram, D.A., Abdelmalak, M.M., Groth, A., Hoffmann, J., Berndt, C., Myklebust, R., 2017. Igneous seismic geomorphology of buried lava fields and coastal escarpments on the Vøring volcanic rifted margin. *Interpretation*, 5, SK161–SK177. https://doi.org/10.1190/INT-2016-0164.1

Planke, S., Rasmussen, T., Rey, S.S., Myklebust, R., 2005. Seismic characteristics and distribution of volcanic intrusions and hydrothermal vent complexes in the Vøring and Møre basins. *Geological Society, London, Petroleum Geology Conference Series*, 6, 833–844. https://doi.org/10.1144/0060833

Prada, M., Sallares, V., Ranero, C.R., Vendrell, M.G., Grevemeyer, I., Zitellini, N., de Franco, R., 2015. The complex 3-D transition from continental crust to backarc magmatism and exhumed mantle in the Central Tyrrhenian basin. *Geophysical Journal International*, 203, 63–78. https://doi.org/10.1093/gji/ggv271

Pubellier, M., Sautter, B., 2022. Key Structural Elements around the East Vietnam Sea (South China Sea) and implications on reconstructions: towards a clarification. *Vietnam Journal of Marine Science and Technology*, 22, 217–229. https://doi.org/10.15625/1859-3097/17435

Pubellier, M., Savva, D., Aurelio, M., Sapin, F., 2016. Structural Map of the South China Sea 1:3000000. Commission for the Geological Map of the World, Paris. https://doi.org/10.14682/2017STRUCTUSCS

Reed, D., 1995. Ship-based Trackline Geophysical Data (MGD77) acquired during the Maurice Ewing expedition EW9509 (1995). *Interdisciplinary Earth Data Alliance (IEDA)*, .

Rizzi, M., Schovsbo, N.H., Hovikoski, J., Nytoft, H.P., Korte, C., Thuy, N.T.T., Bojesen-Koefoed, J., Nielsen, L.H., Abatzis, I., Tuan, N.Q., Toan, D.M., Huyen, N.T., Fyhn, M.B.W., 2021. Carbon isotope stratigraphy in an Oligocene deep syn-rift lake, Gulf of Tonkin, Vietnam: Implications for in-lake isotope fractionation and correlation to the global δ13C trend. *Chemical Geology*, 571, 120179. https://doi.org/10.1016/j.chemgeo.2021.120179

Sandwell, D.T., Müller, R.D., Smith, W.H.F., Garcia, E., Francis, R., 2014. New global marine gravity model from CryoSat-2 and Jason-1 reveals buried tectonic structure. *Science*, 346, 65–67. https://doi.org/10.1126/science.1258213

Sautter, B., Pubellier, M., 2022. Structural control of Mesozoic orogens on SE Asia Basin opening. *Journal of Asian Earth Sciences*, 230, 0–47. https://doi.org/10.1016/j.jseaes.2022.105207

Savva, D., Pubellier, M., Franke, D., Chamot-Rooke, N., Meresse, F., Steuer, S., Auxietre, J.L., 2014. Different expressions of rifting on the South China Sea margins. *Marine and Petroleum Geology*, 58, 579–598. https://doi.org/10.1016/j.marpetgeo.2014.05.023

Schofield, N., Heaton, L., Holford, S.P., Archer, S.G., Jackson, C.A.L., Jolley, D.W., 2012. Seismic imaging of ‘broken bridges’: linking seismic to outcrop-scale investigations of intrusive magma lobes. *Journal of the Geological Society*, 169, 421–426. https://doi.org/10.1144/0016-76492011-150

Scotese, C., 2016. Paleomap Paleoatlas for Gplates and the Paleodataplotter Program. https://doi.org/10.1130/abs/2016nc-275387

Seno, T., 1977. The instantaneous rotation vector of the Philippine sea plate relative to the Eurasian plate. *Tectonophysics*, 42, 209–226. https://doi.org/10.1016/0040-1951(77)90168-8

Shao, L., You, H., Hao, H., Wu, G., Qiao, P., Lei, Y., 2007. Petrology and Depositional Environments of Mesozoic Strata in the Northeastern South China Sea. *Geological Review*, 53.

Shi, H., Xu, C., Zhou, Z., Ma, C., 2011. Zircon U-Pb Dating on Granitoids from the Northern South China Sea and its Geotectonic Relevance. *Acta Geologica Sinica - English Edition*, 85, 1359–1372. https://doi.org/10.1111/j.1755-6724.2011.00592.x

Sibuet, J.C., Hsu, S.K., Debayle, E., 2004. Geodynamic context of the Taiwan orogen. *Geophysical Monograph Series*, 149, 127–158. https://doi.org/10.1029/149GM08

Sibuet, J.C., Hsu, S.K., Le Pichon, X., Le Formal, J.P., Reed, D., Moore, G., Liu, C.S., 2002. East Asia plate tectonics since 15 Ma: Constraints from the Taiwan region. *Tectonophysics*, 344, 103–134. https://doi.org/10.1016/S0040-1951(01)00202-5

Sibuet, J.C., Yeh, Y.C., Lee, C.S., 2016. Geodynamics of the South China Sea. *Tectonophysics*, 692, 98–119.

Smith, A.D., Lewis, C., 2007. Geochemistry of metabasalts and associated metasedimentary rocks from the Lushan Formation of the Upthrust Slate Belt, south-central Taiwan. *International Geology Review*, 49, 1–13. https://doi.org/10.2747/0020-6814.49.1.1

Smith, R.A., 1961. A uniqueness theorem concerning gravity fields. *Mathematical Proceedings of the Cambridge Philosophical Society*, 57, 865–870. https://doi.org/10.1017/S030500410003601X

Sun, Z., Zhou, D., Sun, L., Chen, C., Pang, X., Jiang, J., Fan, H., 2010. Dynamic analysis on rifting stage of Pearl River Mouth basin through analogue modeling. *Journal of Earth Science*, 21, 439–454. https://doi.org/10.1007/s12583-010-0106-0

Talwani, M., 2015. Raw Multi-Channel Seismic Shot Time Navigation Data from the South China Sea acquired during the Vema expedition V3608 (1980). *Interdisciplinary Earth Data Alliance (IEDA)*, . https://doi.org/10.1594/IEDA/321916

Taylor, B., Hayes, D.E., 1983. Origin and history of the South China Sea basin, in: Hayes, D. (Ed.), The Tectonic and Geologic Evolution of the Southeast Asian Seas and Islands, Part 2. American Geophysical Union, , pp. 23–56. https://doi.org/10.1029/GM027p0023

Tian, Z., Tang, W., Wang, P., Zhao, Z., Sun, X., Tang, H., 2021. Tectonic Evolution and Key Geological Issues of the Proto-South China Sea. *Acta Geologica Sinica (English Edition)*, 95, 77–90. https://doi.org/10.1111/1755-6724.14644

Tian, Z., Yan, Y., Huang, C., Zhang, X., Liu, H., Yu, M., Yao, D., Dilek, Y., 2019. Geochemistry and Geochronology of the Accreted Mafic Rocks From the Hengchun Peninsula, Southern Taiwan: Origin and Tectonic Implications. *Journal of Geophysical Research: Solid Earth*, 124, 2469–2491. https://doi.org/10.1029/2018JB016562

Torsvik, T.H., Steinberger, B., Shephard, G.E., Doubrovine, P. V., Gaina, C., Domeier, M., Conrad, C.P., Sager, W.W., 2019. Pacific-Panthalassic Reconstructions: Overview, Errata and the Way Forward. *Geochemistry, Geophysics, Geosystems*, 20, 3659–3689. https://doi.org/10.1029/2019GC008402

Tozer, B., Sandwell, D.T., Smith, W.H.F., Olson, C., Beale, J.R., Wessel, P., 2019. Global Bathymetry and Topography at 15 Arc Sec: SRTM15+. *Earth and Space Science*, 6, 1847–1864. https://doi.org/10.1029/2019EA000658

Wan, K., Xia, S., Cao, J., Sun, J., Xu, H., 2017. Deep seismic structure of the northeastern South China Sea: Origin of a high-velocity layer in the lower crust. *Journal of Geophysical Research: Solid Earth*, 122, 2831–2858. https://doi.org/10.1002/2016JB013481

Wan, X., Li, C.F., Zhao, M., He, E., Liu, S., Qiu, X., Lu, Y., Chen, N., 2019. Seismic Velocity Structure of the Magnetic Quiet Zone and Continent-Ocean Boundary in the Northeastern South China Sea. *Journal of Geophysical Research: Solid Earth*, 124, 11866–11899. https://doi.org/10.1029/2019JB017785

Wang, K.L., Chung, S.L., Lo, Y.M., Lo, C.H., Yang, H.J., Shinjo, R., Lee, T.Y., Wu, J.C., Huang, S.T., 2012a. Age and geochemical characteristics of Paleogene basalts drilled from western Taiwan: Records of initial rifting at the southeastern Eurasian continental margin. *Lithos*, 155, 426–441. https://doi.org/10.1016/j.lithos.2012.10.002

Wang, K.L., Lo, Y.M., Chung, S.L., Lo, C.H., Hsu, S.K., Yang, H.J., Shinjo, R., 2012b. Age and geochemical features of dredged basalts from offshore SW Taiwan: The coincidence of intra-plate magmatism with the spreading South China Sea. *Terrestrial, Atmospheric and Oceanic Sciences*, 23, 657–669. https://doi.org/10.3319/TAO.2012.07.06.01(TT)

Wang, P., Li, Q., Li, C.-F., 2014. Geology of the China Seas, Developments in Marine

Geology. Springer US, Boston, MA.

Wang, P., Prell, W.L., Blum, P., 2000. Leg 184 Summary: Exploring the Asian Monsoon through Drilling in the South China Sea, in: Proceedings of the Ocean Drilling Program, 184 Initial Reports. Ocean Drilling Program, . https://doi.org/10.2973/odp.proc.ir.184.101.2000

Wang, T.K., Chen, M.K., Lee, C.S., Xia, K., 2006. Seismic imaging of the transitional crust across the northeastern margin of the South China Sea. *Tectonophysics*, 412, 237–254. https://doi.org/10.1016/j.tecto.2005.10.039

Wang, Z., Sun, Z., Zhu, J., Guo, M., Jiang, R., 2015. Natural gas geological characteristics and great discovery of large gas fields in deep-water area of the western South China Sea. *Natural Gas Industry B*, 2, 489–498. https://doi.org/10.1016/j.ngib.2016.03.001

Webb, M., Endinanda, F., Gough, A., 2023. Mesozoic magmatism of Natuna Island, Indonesia: Implications for the subduction history of eastern Sundaland. *Gondwana Research*, 119, 45–67. https://doi.org/10.1016/j.gr.2023.02.022

Wei, X.D., Ruan, A.G., Zhao, M.H., Qiu, X.L., Li, J.B., Zhu, J.J., Wu, Z.L., Ding, W.W., 2011. A wide-angle OBS profile across Dongsha Uplift and Chaoshan Depression in the mid-northern South China Sea. *Acta Geophysica Sinica*, 54, 3325–3335. https://doi.org/10.3969/j.issa.0001-5733.2011.12.030

Weilin, Z., Kai, Z., Xiaowei, F., Chunfeng, C., Minqiang, Z., Shunli, G., 2019. The formation and evolution of the East China Sea Shelf Basin: A new view. *Earth-Science Reviews*, 190, 89–111. https://doi.org/10.1016/j.earscirev.2018.12.009

White, R.S., McKenzie, D., O'Nions, R.K., 1992. Oceanic crustal thickness from seismic measurements and rare earth element inversions. *Journal of Geophysical Research*, 97, 19683. https://doi.org/10.1029/92JB01749

Wu, J.-M., 1985. The characteristics of the Geological structures of the Tertiary basins on the continental margin in the northern part of the South China Sea. *Energy*, 10, 359–372. https://doi.org/10.1016/0360-5442(85)90053-2

Xi, W., Jin-fu, D., Yi-han, C., 2005. Distribution Characters and Exploration Potential of Mesozoic Sea Facies Sedimentary Strata in the South China Sea Basin. *Journal of Jilin University: Earth Science Edition*, 35, 456–461.

Xie, X., Ren, J., Pang, X., Lei, C., Chen, H., 2019. Stratigraphic architectures and associated unconformities of Pearl River Mouth basin during rifting and lithospheric breakup of the South China Sea. *Marine Geophysical Research*, 40, 129–144. https://doi.org/10.1007/S11001-019-09378-6/FIGURES/9

Xu, C., Shi, H., Barnes, C.G., Zhou, Z., 2016. Tracing a late Mesozoic magmatic arc along the Southeast Asian margin from the granitoids drilled from the northern South China Sea. *International Geology Review*, 58, 71–94. https://doi.org/10.1080/00206814.2015.1056256

Xu, G., Haq, B.U., 2022. Seismic facies analysis: Past, present and future. *Earth-Science Reviews*, 224, 103876. https://doi.org/10.1016/j.earscirev.2021.103876

Xu, Y., Yan, Q., Shi, X., Jichao, Y., Deng, X., Xu, W., Jing, C., 2022. Discovery of Late Mesozoic volcanic seamounts at the ocean-continent transition zone in the Northeastern margin of South China Sea and its tectonic implication. *Gondwana Research*, . https://doi.org/10.1016/j.gr.2022.04.003

Yan, H., Wang, F., Gu, H., Sun, H., Ge, C., 2020. Geochemical and Sr-Nd-Pb-Hf Isotopic Characteristics of Muchen Pluton in Southeast China, Constrain the Petrogenesis of Alkaline A-Type Magma. *Minerals*, 10, 80. https://doi.org/10.3390/min10010080

Yan, Q., Shi, X., Castillo, P.R., 2014. The late Mesozoic-Cenozoic tectonic evolution of the South China Sea: A petrologic perspective. *Journal of Asian Earth Sciences*, 85, 178–201. https://doi.org/10.1016/j.jseaes.2014.02.005

Ye, Q., Mei, L., Shi, H., Camanni, G., Shu, Y., Wu, J., Yu, L., Deng, P., Li, G., 2018. The Late Cretaceous tectonic evolution of the South China Sea area: An overview, and new perspectives from 3D seismic reflection data. *Earth-Science Reviews*, 187, 186–204. https://doi.org/10.1016/j.earscirev.2018.09.013

Yeh, Y.C., Hsu, S.K., Doo, W. Bin, Sibuet, J.C., Liu, C.S., Lee, C.S., 2012. Crustal features of the northeastern South China Sea: Insights from seismic and magnetic interpretations. *Marine Geophysical Research*, 33, 307–326. https://doi.org/10.1007/s11001-012-9154-4

Yeh, Y.C., Sibuet, J.C., Hsu, S.K., Liu, C.S., 2010. Tectonic evolution of the Northeastern South China Sea from seismic interpretation. *Journal of Geophysical Research: Solid Earth*, 115. https://doi.org/10.1029/2009JB006354

Yeh, Y.H., Shih, R.C., Lin, C.H., Liu, C.C., Yen, H.Y., Huang, B.S., Liu, C.S., Chen, P.Z., Huang, C.S., Wu, C.J., Wu, F.T., 1998. Onshore/Offshore Wide-Angle Deep Seismic Profiling in Taiwan. *Terrestrial, Atmospheric and Oceanic Sciences*, 9, 301–316. https://doi.org/10.3319/TAO.1998.9.3.301(TAICRUST)

Young, A., Flament, N., Maloney, K., Williams, S., Matthews, K., Zahirovic, S., Müller, R.D., 2019. Global kinematics of tectonic plates and subduction zones since the late Paleozoic Era. *Geoscience Frontiers*, 10, 989–1013. https://doi.org/10.1016/j.gsf.2018.05.011

Yu, S.-B., Chen, H.-Y., Kuo, L.-C., 1997. Velocity field of GPS stations in the Taiwan area. *Tectonophysics*, 274, 41–59. https://doi.org/10.1016/S0040-1951(96)00297-1

Zhang, Q., Wu, S., Dong, D., 2016. Cenozoic magmatism in the northern continental margin of the South China Sea: evidence from seismic profiles. *Marine Geophysical Research*, 37, 71–94. https://doi.org/10.1007/s11001-016-9266-3

Zhao, M., Qiu, X., Xia, S., Xu, H., Wang, P., Wang, T.K., Lee, C.-S., Xia, K., 2010. Seismic structure in the northeastern South China Sea: S-wave velocity and Vp/Vs ratios derived from three-component OBS data. *Tectonophysics*, 480, 183–197. https://doi.org/10.1016/j.tecto.2009.10.004

Zhong, L.F., Cai, G.Q., Koppers, A.A.P., Xu, Y.G., Xu, H.H., Gao, H.F., Xia, B., 2018. 40Ar/39Ar dating of oceanic plagiogranite: Constraints on the initiation of seafloor spreading in the South China Sea. *Lithos*, 302–303, 421–426. https://doi.org/10.1016/j.lithos.2018.01.018

Zhou, D., 2002. Mesozoic strata and sedimentary environment in SW Taiwan Basin of NE South China Sea and Peikang high of western Taiwan. *Journal of Tropical Oceanography*, 21, 50–57.

Zhou, D., Sun, Z., Chen, H.Z., Xu, H.H., Wang, W.Y., Pang, X., Cai, D.S., Hu, D.K., 2008. Mesozoic paleogeography and tectonic evolution of South China Sea and adjacent areas in the context of Tethyan and Paleo-Pacific interconnections. *Island Arc*, 17, 186–207. https://doi.org/10.1111/j.1440-1738.2008.00611.x